Langmuir

Article

pubs.acs.org/Langmuir

Entropic Separation of Styrene/Ethylbenzene Mixtures by Exploitation of Subtle Differences in Molecular Configurations in Ordered Crystalline Nanoporous Adsorbents

Ariana Torres-Knoop,* Jurn Heinen, Rajamani Krishna, and David Dubbeldam

Van 't Hoff Institute for Molecular Sciences, University of Amsterdam, Science Park 904, 1098 XH Amsterdam, The Netherlands

Supporting Information

ABSTRACT: The separation of styrene/ethylbenzene mixture is of great importance in the petrochemical industry. Current technology uses distillation; this separation is difficult because of the small, 9 K, difference in the boiling points. An alternative separation method uses selective adsorption in nanoporous materials such as zeolites and metal−organic frameworks. Here we present a simulation screening study for the separation of styrene/ethylbenzene mixture by adsorptive means in nanoporous materials near pore saturation conditions. Under these conditions, different entropic mechanisms can dictate the separation process. Commensurate stacking has the best trade-off between selectivity and saturation capacity and offers a geometrical solution to the separation problem. MIL-47 has the right channel size and topology for styrene to exhibit commensurate stacking offering high capacity and selectivity for styrene over ethylbenzene. Out of all the screened structures, MIL-47 was found to be the best candidate for the separation of styrene/ethylbenzene mixture.

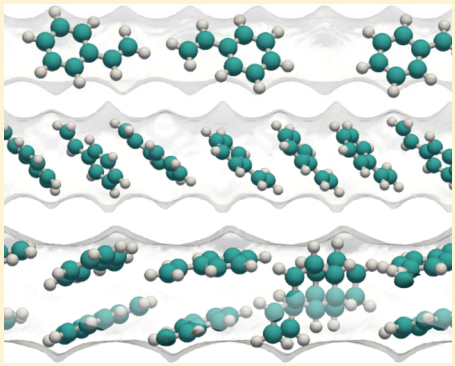

INTRODUCTION

Styrene is an important feedstock in the petrochemical industry. The reactivity of its vinyl group makes styrene easy to polymerize and copolymerize, and therefore, it serves as raw material for the production of a great variety of materials, with the two most important being polystyrene and rubber.[1] Although styrene appears in small quantities in nature, the global consumption (of the order of millions of tons per year) requires its commercial production. There are two main methods to obtain styrene: dehydrogenation of ethylbenzene and coproduction of styrene and propylene oxide via hydroperoxidation of ethylbenzene. Direct dehydrogenation of ethylbenzene to styrene accounts for the majority of the production. The conventional method involves two steps: the alkylation of benzene with ethylene to produce ethylbenzene and the dehydrogenation of the ethylbenzene to produce styrene. Complete conversion is not achieved in the reactor, and therefore, the product stream contains a large fraction of ethylbenzene that has to be removed.

The preferred technology for the separation of ethylbenzene from styrene nowadays is extractive distillation[2] and vacuum distillation[3,4] together with inhibitors like phenylene-diamines or dinitrophenols to avoid styrene from polymerizing. However, because of the similarity in the boiling point of styrene (418 K) and ethylbenzene (409 K), this process is energetically expensive and most of the energy needed for the production of styrene is used in the separation process. The process is even more complicated due of the presence of side products like toluene, *o*-xylene, and benzene.

An alternative energy-efficient separation strategy involves utilizing the molecular, chemical, and geometrical differences by means of adsorptive separation with nanoporous materials like metal−organic frameworks and zeolites. Ahmad et al.[5] performed liquid chromatography separation using HKUST-1($Cu_3(BTC)_2$) a metal−organic framework with open Cu(II) sites and BTC(1,3,5-benzenetricarboxylate) linkers. They found that styrene is preferentially adsorbed in the structure because of the coordinative interaction of styrene with the Cu(II) in a π-complexation mechanism. Maes et al.[6,7] and Remy et al.[8] reported results on MIL-47(V) and MIL-53(Al), showing both structures are capable of separation in the liquid phase. They found that in MIL-47(V) styrene selectivity is related to styrene capacity for packing, while for MIL-53(Al) styrene selectivity is related to adsorption enthalpy (interaction with the carboxylate). For competitive adsorption in static conditions, they reported separation factors of 3.6 and 4.1 for MIL-47(V) and MIL-53(Al), respectively, and for an equimolar mixture in dynamic conditions (breakthrough experiments using a column filled with crystallites in an HPLC apparatus) they found separation factors of 2.9 and 2.3. They also observed that if a more realistic mixture is taken into account (with toluene and *o*-xylene) in MIL-53, *o*-xylene and toluene are retained even longer, which makes the material good for impurity removal. Yang and Yan[9] conducted experiments on stationary phase HPLC with MIL-101(Cr), a material built

Received: January 29, 2015
Revised: March 2, 2015
Published: March 12, 2015

DOI: 10.1021/acs.langmuir.5b00363
Langmuir 2015, 31, 3771−3778

from a hybrid supertetrahedral building unit formed by terephthalate ligands and trimeric chromium octahedral clusters. Similar to the case of HKUST-1, they reported a higher affinity toward styrene due to the $\pi-\pi$ interactions with the metal−organic framework walls and the unsaturated metal sites. They also reported the efficient separation of impurities like *o*-xylene and toluene.

Separation based on adsorption relies on either adsorption or diffusion characteristics. At low loadings (i.e., the Henry regime), the selectivity is mainly driven by enthalpic effects, and favors the molecule with the strongest interaction with the framework. Selectivity is therefore strongly related to adsorbent and adsorbate properties such as dipole moment, polarizability, quadrupole moment, and magnetic susceptibility. At saturation conditions (industrial setup), the selectivity is driven by either enthalpic effects and/or entropic effects, like (i) "commensurate freezing",[10] which favors molecules for which size is commensurate with the channel; (ii) "size entropy",[11,12] which favors the smallest molecules; (iii) "length entropy",[11,13−15] which favors the molecules with the shortest effective length (footprint) in one-dimensional (1D) channels; (iv) "commensurate stacking",[16] which favors molecules with stacking arrangements that are commensurate with the dimensions of one-dimensional channels; (v) "face-to-face stacking",[17] which favors molecules that, when reoriented, significantly reduce their footprint in one-dimensional channels.

The various separation strategies for exploitation of molecular packing effects have been reviewed recently.[18]

Styrene and ethylbenzene are very similar molecules, with the main difference being that styrene is a flat molecule whereas ethylbenzene is not. Finding structures with selective adsorption for styrene is not easy. In this work, we present a screening study for the separation of styrene and ethylbenzene at liquid conditions. We propose to separate on the basis of a difference in saturation loading because it is more cost-efficient and utilizes the pore volume most efficiently.

METHODOLOGY SECTION

Methodology. The systems were modeled using classical force fields. The adsorbates were modeled with OPLS-AA force field for organic liquids.[19] In previous work[16] we have shown that the use of these force fields is in good agreement with experiments. Because we were interested in the selectivity of planar/nonplanar molecules and not in their conformational changes, adsorbates were described as multisite rigid molecules with properties and configurations shown in Figure 1. The parameters for the interaction of the adsorbates (Lennard−Jones and electrostatic interactions) together with a schematic representation of the molecules showing the atom types are presented in Table 1. Cross-interactions with other molecules and the framework were computed using Lorentz−Berthelot mixing rules.

The frameworks were modeled as rigid with atom positions taken from crystallographic experimental data. Most MOFs were further optimized using VASP[23,24] with the cell fixed to the experimentally determined unit cell size and shape (PBE[25,26] exchange-correlation functional with dispersion corrections[27] was used and the PAW method was applied to describe the core atoms; convergence criteria of the ionic forces was set to 1×10^3 eV/Å). The metal−organic frameworks were modeled using the DREIDING force field,[28] and van der Waals parameters not found in DREIDING were taken from the universal force field (UFF).[29] DREIDING and UFF force fields were designed to be very generic, so that broad coverage of the periodic table, including inorganic compounds, metals, and transition metals, could be achieved. UFF was tailored for simulating molecules containing any combination of elements in the periodic table. For

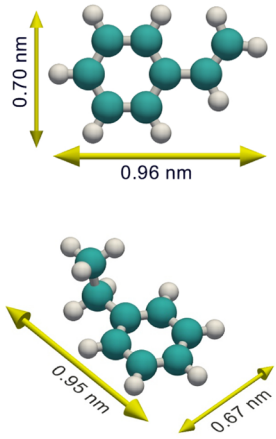

Boiling point	418 K
Freezing point	242.5 K
length	0.96 nm
width	0.70 nm
height	0.34 nm

Boiling point	409 K
Freezing point	178 K
length	0.95 nm
width	0.67 nm
height	0.53 nm

Figure 1. Styrene (top) and ethylbenzene (bottom) configurations. The figure shows the typical properties of the modeled adsorbates. Distances are "molecular shadow lengths"[20] from Materials Studio.[21] Besides small differences in the charges, the main difference between these molecules is their height (planarity).

Table 1. OPLS-AA Force Field Parameters for Styrene and Ethylbenzene[19a]

atom/group	q [e$^-$]	σ [Å]	ε [kcal mol^{-1}]
C	-0.115	3.55	0.070
C1	-0.115	3.55	0.076
C2	-0.005	3.50	0.066
C3	-0.180	3.50	0.066
C4	-0.000	3.55	0.076
C5	-0.115	3.55	0.076
C6	-0.148*	3.55	0.076
H	0.115	2.42	0.030
H1	0.060	2.42	0.030
H2	0.074*	2.42	0.030

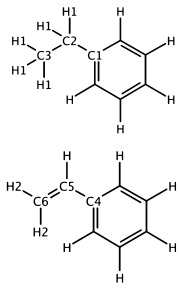

[a]The vinyl group charges (*) were taken from Siu et al.[22]

the zeolites, the TraPPE[30] force field was used. This force field was specifically developed for zeolites.

The charge−charge interactions were computed using the Ewald summation (relative precision 10^{-6}). Charges for the frameworks were computed by minimizing the difference of the classical electrostatic potential and a quantum mechanics electrostatic potential over many grid points using the REPEAT method.[31,32]

Adsorption Isotherms. To compute the adsorption isotherms, we performed Monte Carlo simulation in the grand-canonical ensemble (or μ,V,T ensemble). In this ensemble, the number of adsorbates fluctuates until equilibrium conditions are reached: the temperature and chemical potential of the gas inside and outside the adsorbent are equal. Because in confined systems the fraction of successful insertions and deletions is very low, reaching equilibrium with conventional Monte Carlo methods can be very time-consuming. In this study, we used the Configurational Bias Continuous Fractional Monte Carlo (CB/CFCMC)[33] method to enhance the success rate of insertions and deletions. The method is a combination of the Configurational Bias Monte Carlo (CBMC),[34−36] where molecular growth is biased toward favorable configurations, and Continuous Fractional Component Monte Carlo (CFCMC),[37] in which molecules are gradually inserted or deleted by scaling their interactions with the surroundings. We have shown in previous work[33] that the results obtained with this method do not differ from CBMC calculations but the efficiency is higher. More details can be found in the Supporting Information.

Using the dual-site Langmuir−Freundlich fits of the pure component isotherms, breakthrough calculations were carried out by solving a set of partial differential equations for each of the species in the gas mixture.[38,39] The molar loadings of the species at any position along the packed bed and at any time were determined from Ideal

DOI: 10.1021/acs.langmuir.5b00363
Langmuir 2015, 31, 3771−3778

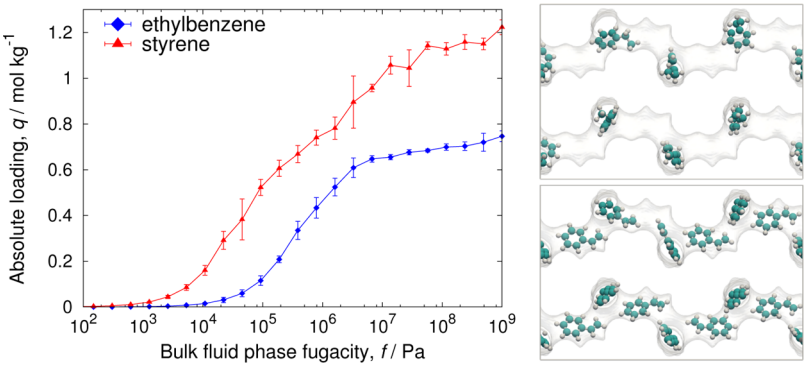

Figure 2. (a) Simulated single component isotherms of styrene and ethylbenzene in MFI-para at 433 K. (b) Snapshot of ethylbenzene (top) and styrene (bottom) at 1×10^9 Pa and 433 K.

Adsorbed Solution Theory calculations. Video animations of the breakthrough behavior as a function of time of selected structures are available in the Supporting Information.

RESULTS

We perform a screening study of several zeolites and metal–organic frameworks for the separation of styrene/ethylbenzene mixture focusing on saturation conditions. Under these conditions, differences in the saturation capacity of the mixture components strongly dictate the separation.

In systems with small pores, like MRE and MTW zeolites, molecules are forced to adsorb parallel to the channels. The saturation capacity is determined by the effective length per molecule in the channel (*footprint*). Because of the similarity in the length of styrene and ethylbenzene, the difference in saturation capacities is almost negligible, making systems with small pores unsuitable candidates for the separation.

In structures with cavities or channels much larger than styrene and ethylbenzene molecular dimensions, like IRMOF-1 and Zn-DOBDC, molecules do not present any particular packing. The observed difference in the saturation capacities is a consequence of the natural packing of the molecules in liquid phase (ρ_{Eb} = 0.8665 g/mL, ρ_{St} = 0.909 g/mL). This makes these materials also unsuitable for the separation process.

We have identified a few materials where styrene has a higher saturation capacity than ethylbenzene. In the following we describe how this difference arises from the previously mentioned entropic mechanisms and we highlight their applicability for the separation process.

Size Exclusion. is observed in MFI-para.[40] MFI-para is a ZSM-5 zeolite which structure is a combination of interconnected straight and zigzag channels. The straight channels have a diameter of 5.3 × 5.6 Å and the zigzag channels have a diameter of 5.1 × 5.5 Å. In Figure 2 the simulated single component isotherms of styrene and ethylbenzene in MFI-para at 433 K and snapshots of styrene and ethylbenzene at 1×10^9 Pa and 433 K are presented. At low loadings molecules preferentially adsorb in the straight channels, the difference in loadings arise from a stronger interaction of styrene with MFI-para. At saturation conditions, styrene can obtain almost twice the loading of ethylbenzene because of a size exclusion effect in the zigzag channels in which ethylbenzene does not fit due to its height. When an equimolar styrene/ethylbenzene mixture is considered, the difference in loadings at saturation conditions is even larger (Supporting Information Figure S2b). Breakthrough simulations confirm the strong styrene selectivity of MFI-para (Figures S3).

Face-to-Face Stacking. Face to-face stacking occurs in MAZ[41] and AFI[42] zeolites. MAZ and AFI are 1D-channel zeolites with dimensions that allow a molecular reorientation of ethylbenzene and styrene.

In Figure 3, we present the simulation results for the single component isotherms of ethylbenzene and styrene in AFI

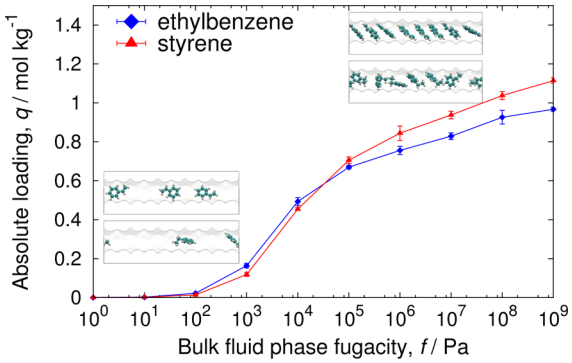

Figure 3. Single component isotherms of styrene and ethylbenzene in AFI at 433 K. Inset: Snapshots of styrene (top) and ethylbenzene (bottom) at 1×10^3 and 1×10^9 Pa. At low loadings, both molecules are adsorbed with the phenyl group parallel to the channel axis. At higher pressures, styrene can arrange in a tilted face-to-face stacking configuration, which reduces its footprint and allows for a higher saturation capacity. The difference in saturation capacities ensures the selectivity of AFI toward styrene at saturation conditions in the mixture.

zeolite at 433 K. At low loadings, molecules are mostly adsorbed flat on the walls (parallel to the channels axis), and adsorption is dictated by enthalpy effects, which favors ethylbenzene. As the loading increases, the molecules undergo a molecular reorientation from a configuration parallel to the channel axis to a "pile" configuration with the phenyl groups facing each other. This new configuration (face-to-face stacking) reduces styrene's footprint more than ethylbenzene's footprint (Figure 4a) because of the nonplanarity of ethylbenzene, allowing styrene to obtain higher saturation loadings.

For MAZ zeolite, a similar behavior is observed; however, because MAZ zeolite has smaller channels than AFI does, the angle at which molecules can reorient has a smaller effect on the reduction of the molecule's footprint in the channels

DOI: 10.1021/acs.langmuir.5b00363
Langmuir 2015, 31, 3771−3778

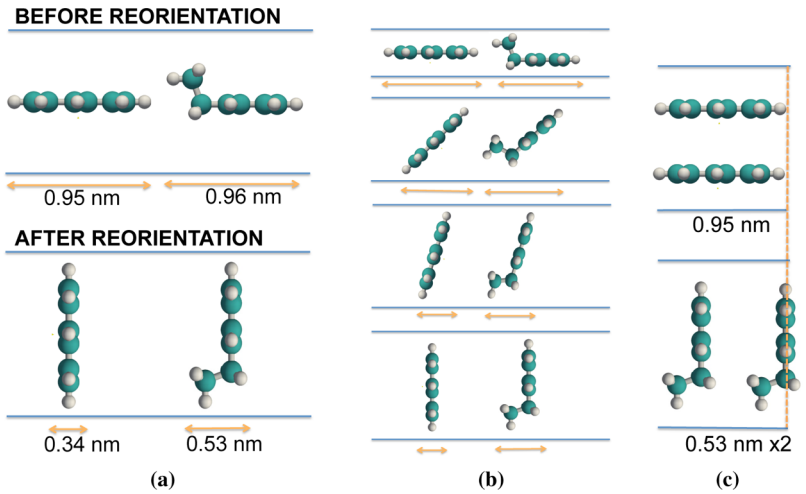

Figure 4. Schematic representation of different entropic effects occurring in the separation of styrene and ethylbenzene in nanoporous materials. (a) The reduction of the molecule's footprint in the channels because of a reorientation into a face-to-face stacking configuration. (b) Effect of the channel size on the reorientation and therefore molecule's footprint reduction. (c) Comparison of the channel length needed for two molecules of styrene to have commensurate stacking vs two molecules of ethylbenzene to have face-to-face stacking.

(Figure 4b). When an equimolar mixture is considered, both AFI and MAZ zeolites are styrene selective at saturation conditions as shown in Figures S5b and S8b where the simulated mixture component isotherms at 433 K are presented.

Face-to-face stacking is also observed in DON zeolite. DON[43] is a structure with 1D-channels slightly larger than those of AFI and MAZ zeolites. This increase in dimensions favors ethylbenzene to undergo a molecular reorientation into a face-to-face stacking configuration but also, because the diameter of the channels are larger than the length of styrene, it induces styrene to adopt a "commensurate stacking" configuration where the stacking of two molecules with their phenyl groups facing each other is commensurate with the channel dimensions (Figure S10). This is also observed in MIL-53,[44] a metal−organic framework with lozenge-shaped rhombohedric channels of approximately 0.85 nm, as shown in Figure S13 where snapshots of styrene and ethylbenzene at 1 × 10^9 Pa and 433 K are presented. Because of styrene and ethylbenzene dimensions, styrene with commensurate stacking can obtain higher saturation capacities than ethylbenzene with face-to-face stacking as shown schematically in Figure 4c. This is also seen in DON and MIL-53 single component isotherms (Figures S11a and S14a). Mixture isotherms (Figures S11b and S14b) and breakthrough curves (Figures S12 and S15) further confirm that DON and MIL-53 are styrene selective structures.

Commensurate Stacking. Commensurate stacking for both styrene and ethylbenzene is observed in MIL-47[45] and MAF-X8.[46] MIL-47 is a metal−organic framework with lozenge-shaped rhombohedric channels which size (slightly larger than MIL-53) allows for ethylbenzene to also have commensurate stacking. In Figure 5 we present the simulated single component adsorption isotherms of ethylbenzene and styrene in MIL-47 at 433 K and snapshots of styrene and ethylbenzene at 1 × 10^6 Pa and 1 × 10^9 Pa. At 1 × 10^9 Pa both molecules have commensurate stacking, but in order for ethylbenzene to have commensurate stacking the phenyl groups have to be slightly shifted due to the nonplanar ethyl group. This shift affects the amount of ethylbenzene molecules that can be adsorbed (as compared to styrene) and therefore causes a difference in the saturation capacity of styrene and

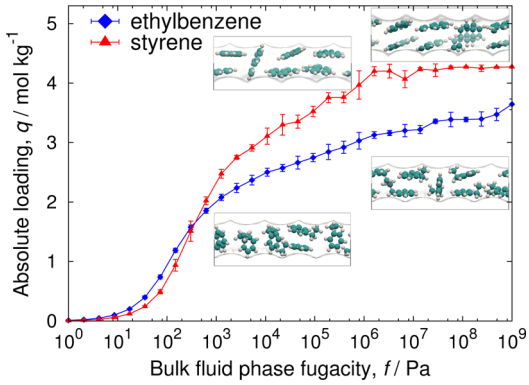

Figure 5. Single component adsorption isotherms for styrene and ethylbenzene at 433 K in MIL-47. Inset: Styrene (top) and ethylbenzene (bottom) snapshots at 1 × 10^6 and 1 × 10^9 Pa. Styrene has commensurate staking at lower pressures than ethylbenzene. Because of the out of plane ethyl group, ethylbenzene molecules have to be slightly shifted in order to have commensurate stacking and therefore less ethylbenzene molecules can be adsorbed in MIL-47 channels at saturation conditions.

ethylbenzene. Interestingly, commensurate stacking occurs at lower loading for styrene than for ethylbenzene. We can see in Figure 5 that at 1 × 10^6 Pa styrene already presents commensurate stacking while ethylbenzene seems to have more of a face-to-face stacking. In a mixture, this will favor styrene adsorption even more. In Figure 6, simulated mixture adsorption isotherms for an equimolar mixture in MIL-47 at 433 K are presented. MIL-47 is a styrene selective structure. Our results are in good qualitative agreement with Maes et al.[6] Breakthrough simulations further confirm that MIL-47 is a styrene selective structure at saturation conditions.

In MAF-x8, a metal−organic framework with square channels of approximately 1 nm, it is easier for ethylbenzene to have commensurate stacking than in MIL-47. The single component isotherms of both molecules behave in a very similar manner. The topology of the structure seems to induce a shift between parallel styrene molecules and allows for the ethyl group of ethylbenzene to stick in the channel "pockets" (Figure S19). This might be the reason for the smaller

DOI: 10.1021/acs.langmuir.5b00363
Langmuir 2015, 31, 3771−3778

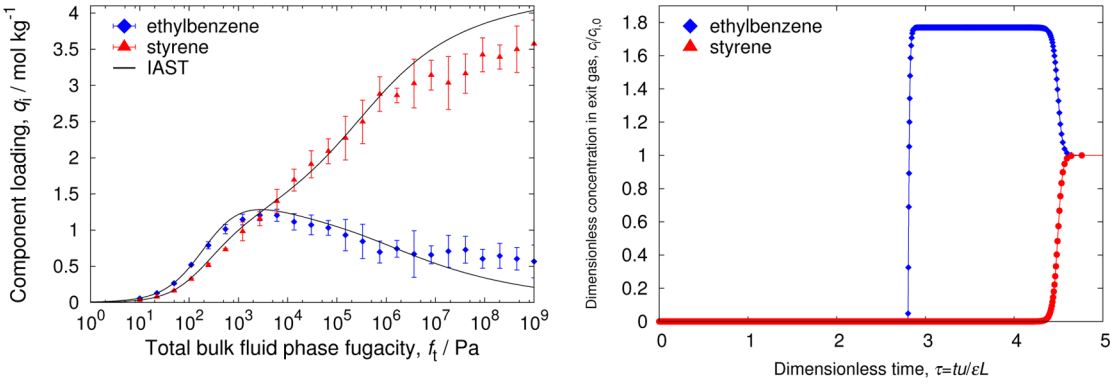

(a) (b)

Figure 6. Styrene/ethylbenzene separation using MIL-47 at 433 K. (a) Equimolar mixture isotherms and Ideal Adsorption Solution Theory (IAST) prediction based on pure component isotherms. (b) Simulated step breakthrough at 1 × 10^6 Pa total fugacity. The IAST prediction is in excellent agreement with the mixture simulations. The mixture and breakthrough simulations show a high styrene selectivity and loading in the mixture.

difference in saturation capacities of styrene and ethylbenzene compared to MIL-47.

Combination/Competition of Mechanisms. Combination/competition of mechanisms is observed in structures with a more complex topology. An example of this is MOF-CJ3 metal−organic framework.[47] The wide segment of the channels are big enough to allow for both styrene and ethylbenzene to form two parallel rows (commensurate stacking); however, the shape of the channels forces ethylbenzene molecules to adopt a configuration where the ethyl group is pointing to the channel "pockets". Styrene has more freedom and molecules can arrange in a way that an extra styrene can be adsorb in the protracted segments in a configuration perpendicular to the channel (face-to-face stacking) (Figure 7). The interplay between different mechanisms rarely makes the separation better. Even when all the mechanisms favor a specific molecule, the competition between them can induce enough disorder to destroy the selectivity one could achieve with a "pure"-mechanism.

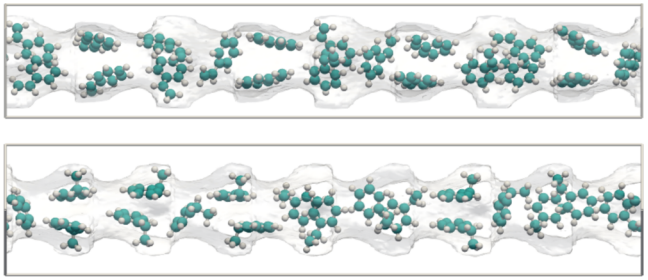

Figure 7. Snapshots of styrene (top) and ethylbenzene (bottom) at 1 × 10^9 Pa and 433 K in MOF-CJ3.

DISCUSSION

There are two important factors to consider when using adsorption for separation processes at industrial conditions, namely, selectivity and capacity. A high selectivity ensures that less cycles are needed to achieve a high degree of purity in the separation, but a high capacity implies that the regeneration time is longer. For a binary mixture, the adsorption selectivity is defined as

$$S_{ads} = \frac{q_1/q_2}{f_1/f_2} \quad (1)$$

and the capacity is defined as the styrene loading in the adsorbed phase of a binary mixture.

$$\text{capacity} = q_1 \quad (2)$$

In Figure 8, the relationship between these two properties for different structures is presented. Structures with the same separation mechanism are plotted with the same color. An ideal structure for the separation would be located at the right top corner.

In structures where the separation is driven by size-exclusion (MFI-para), the selectivity is high because there is an

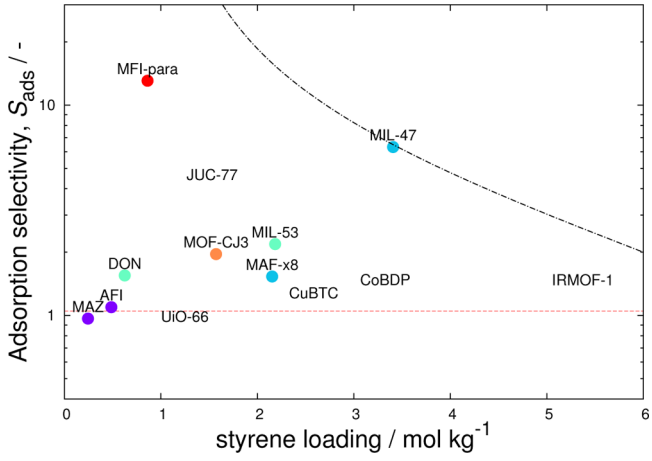

Figure 8. Selectivity as a function of styrene loading (capacity) in a binary mixture at 433 K and 1 × 10^6 Pa total fugacity. The structures are divided in different colors depending on the selectivity mechanism observed. Color code: Size exclusion (red), face-to-face stacking (purple), commensurate stacking (blue), commensurate-stacking/face-to-face stacking (green), and mixed (orange). The dotted red line corresponds to the ratio styrene/ethylbenzene at liquid conditions. There is a natural trade-off between selectivity and loading, and finding structures in the top right corner is not feasible. The black dashed line (guide to the eye) denotes the inverse relationship between selectivity and capacity. MIL-47 is a styrene selective material with a high capacity and therefore a good candidate for the styrene/ethylbenzene separation.

DOI: 10.1021/acs.langmuir.5b00363
Langmuir 2015, 31, 3771−3778

adsorption site available only for styrene (zigzag channels), but the capacity is rather low since for size-exclusion to occur among similar molecules, there has to be a very tight fit between the molecules and the adsorbent, usually associated with small pore systems.

In structures where the separation is driven by face-to-face stacking, the selectivity relies on the increase of the molecule's footprint difference, consequence of a reorientation, and piling. Ideally, only one of the mixture components should be able to reorient, but in the case of styrene and ethylbenzene the similarity in their length and width makes no significant difference in the pore size needed for the reorientation. The selectivity relies thus on how favorable the reorientation and piling are.

In MAZ and AFI, both molecules can reorient but the reorientation is restricted by the pore size, forcing a tilting in the face-to-face stacking configuration that is unfavorable for ethylbenzene to form a pile but it is favorable for styrene. This allows styrene to obtain higher saturation loadings and ensures MAZ and AFI styrene selectivity at saturation conditions.

However, face-to-face stacking only occurs at high loadings. In Figure 8, the selectivity is presented at 1×10^6 Pa; at this fugacity, MAZ is not yet styrene selective and AFI selectivity is almost negligible. The effect of face-to-face stacking in styrene selectivity can only be observed at higher loadings as shown in Figure S30, where the selectivity as a function of styrene loading for higher fugacities is presented. Face-to-face stacking can only occur when the reoriented molecules are commensurate with the channel diameter. This has an important restriction in the pore size and therefore in the capacity.

In structures where styrene has commensurate stacking and ethylbenzene has face-to-face stacking (as observed in MIL-53 and DON), the difference in saturation capacities arises because the channel length needed to accommodate molecules of styrene in commensurate stacking is smaller than the channel length needed to accommodate molecules of ethylbenzene in face-to-face stacking. When an equimolar mixture is considered, styrene will be favored even more because it does not have to undergo any reorientation to achieve higher loadings. Structures with pore sizes that allow styrene to have commensurate stacking, but not ethylbenzne, are styrene selective and have a higher saturation capacity than structures that present face-to-face stacking or size exclusion.

In structures where both styrene and ethylbenzene can have commensurate stacking (MIL-47 and MAF-x8), the selectivity will depend on the efficiency in which the molecules can stack. In Figure 9, we present a schematic of commensurate stacking configurations of styrene and ethylbenzene. For ethylbenzene to have commensurate stacking, the "minimal length", the "packing length", or both have to be larger than that for styrene. At saturation conditions, this implies that more styrene molecules can be adsorbed than ethylbenzene ones, favoring the adsorption of styrene over ethylbenzene in a mixture. Commensurate stacking enhances the dimensional differences of styrene and ethylbenzene as "pairs" of molecules. Because commensurate stacking occurs in structures with larger pores, high capacity can be attained.

Commensurate stacking is the best mechanism for the separation of ethylbenzene and styrene. It offers a geometrical solution to the separation problem that ensures a high selectivity, and it occurs in open pore structures, ensuring a high capacity. The channel topology can facilitate or impede the selectivity.

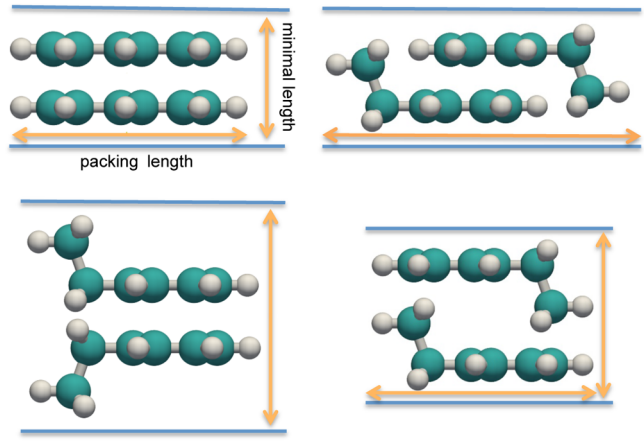

Figure 9. Schematic differences of the channel dimensions needed for commensurate stacking. Because styrene is a planar molecule, commensurate stacking can occur in smaller channels. Commensurate stacking is a powerful separation mechanism for planar/nonplanar molecules.

In the case of MIL-47, the almost planar walls force ethylbenzene molecules to be shifted, increasing the difference in "length" per pair of molecules in the channel as compared to styrene. This makes MIL-47 a highly styrene selective material and the best candidate for the separation of styrene/ethylbenzene from the structures we screened.

CONCLUSION

Styrene and ethylbenzene are very similar molecules, and finding structures that can discriminate between them is not easy. At liquid conditions, the success in the separation process is strongly related to the difference in saturation capacities of the mixture components which in turn is strongly dictated by the underlying entropic mechanisms occurring in the nanoporous material. Commensurate stacking offers the best trade-off between saturation capacity and selectivity and is therefore a very efficient mechanism for the separation of styrene and ethylbenzene. Among the different structures we studied, MIL-47, a styrene selective structure, is the best candidate for the adsorptive separation of styrene/ethylbenzene mixture in nanoporous materials. Commensurate stacking offers a geometrical solution to the separation of planar/nonplanar molecules, and this enables a convenient approach to designing materials for the separation.

ASSOCIATED CONTENT

Supporting Information

Structural details of various materials investigated, pure component and mixture adsorption data, dual-Langmuir–Freundlich fits parameters for unary isotherms, and transient breakthrough simulation results for various materials. Video animations of the breakthroughs in various microporous adsorbents operating at a total pressure of 100 kPa and 433 K. This material is available free of charge via the Internet at http://pubs.acs.org.

AUTHOR INFORMATION

Corresponding Author

*E-mail: A.TorresKnoop@uva.nl.

Notes

The authors declare no competing financial interest.

DOI: 10.1021/acs.langmuir.5b00363
Langmuir 2015, 31, 3771−3778

■ ACKNOWLEDGMENTS

This material is supported by The Netherlands Research Council for Chemical Sciences (NWO-CW), also through a VIDI grant (D.D.), and by the Stichting Nationale Computerfaciliteiten (National Computing Facilities Foundation, NCF) for the use of supercomputing facilities.

■ REFERENCES

(1) Wunsch, J. *Polystyrene: Sythesis, Production and Applications*; Rapra Technology Ltd.: Telford, UK, 2000.
(2) Gentry, J. C.; Kumar, S.; Wright-Wytcherley, R. Use Extractive Distillation to Simplify Petrochemical Processes. *Hydrocarbon Process.* **2004**, *93*, 62−66.
(3) Randall, G. Method of Separating Ethylbenzene from Styrene by Low Pressure Drop Distillation. U.S. Patent 3.084.108, 1963; http://www.google.com/patents/US3084108.
(4) van Tassell, H. Separation of Ethylbenzene and Styrene by Low Pressure. High Temperature Distillation. U.S. Patent 3.398.063, 1968; http://www.google.com/patents/US3398063.
(5) Ahmad, R.; Wong-Foy, A. G.; Matzger, A. J. Microporous Coordination Polymers as Selective Sorbents for Liquid Chromatography. *Langmuir* **2009**, *25*, 11977−9.
(6) Maes, M.; Alaerts, L.; Vermoortele, F.; Ameloot, R.; Couck, S.; Finsy, V.; Denayer, J. F. M.; De Vos, D. E. Separation of C5-hydrocarbons on Microporous Materials: Complementary Performance of MOFs and Zeolites. *J. Am. Chem. Soc.* **2010**, *132*, 2284−2292.
(7) Maes, M.; Vermoortele, F.; Alaerts, L.; Couck, S.; Kirschhock, C. E. A.; Denayer, J. F. M.; De Vos, D. E. Separation of Styrene and Ethylbenzene on Metal-Organic Frameworks: Analogous Structures with Different Adsorption Mechanisms. *J. Am. Chem. Soc.* **2010**, *132*, 15277−15285.
(8) Remy, T.; Ma, L.; Maes, M.; Vos, D. E. D.; Baron, G. V.; Denayer, J. F. M. Vapor-Phase Adsorption and Separation of Ethylbenzene and Styrene on the Metal-Organic Frameworks MIL-47 and MIL-53(Al). *Ind. Eng. Chem. Res.* **2012**, *5*, 14824−14833.
(9) Yang, C.-X.; Yan, X.-P. Metal-Organic Framework MIL-101(Cr) for High-Performance Liquid Chromatographic Separation of Substituted Aromatics. *Anal. Chem.* **2011**, 7144−7150.
(10) Smit, B.; Maesen, T. Commensurate "Freezing" of Alkanes in the Channels of a Zeolite. *Nature* **1994**, *374*, 42−44.
(11) Talbot, J. Analysis of Adsorption Selectivity in a One-Dimensional Model System. *AIChE. J.* **1997**, *43*, 2471−2478.
(12) Du, Z.; Manos, G.; Vlugt, T.; Smit, B. Molecular Simulation of Adsorption of Short Linear Alkanes and Their Mixtures in Silicalite. *AIChE. J.* **1998**, *44*, 1756−1764.
(13) van Baten, J. M.; Krishna, R. Entropy Effects in Adsorption and Diffusion of Alkane Isomers in Mordenite: An Investigation using CBMC and MD simulations. *Microporous Mesoporous Mater.* **2005**, *84*, 179−191.
(14) Krishna, R.; Smit, B.; Calero, S. Entropy Effects During Sorption of Alkanes in Zeolites. *Chem. Soc. Rev.* **2002**, *31*, 185−194.
(15) Krishna, R.; van Baten, J. M. In Silico Screening of Metal-Organic Frameworks in Separation Applications. *Phys. Chem. Chem. Phys.* **2011**, *13*, 10593−10616.
(16) Torres-Knoop, A.; Krishna, R.; Dubbeldam, D. Separating Xylene Isomers by Commensurate Stacking of p-Xylene within Channels of MAF-X8. *Angew. Chem. Int.* **2014**, *53*, 7774−7778.
(17) Torres-Knoop, A.; Balestra, S. R. G.; Krishna, R.; Calero, S.; Dubbeldam, D. Entropic Separations of Mixtures of Aromatics by Selective Face-to-Face Molecular Stacking in One-Dimensional Channels of Metal-Organic Frameworks and Zeolites. *Chem. Phys. Chem.* **2015**, *16*, 532−535.
(18) Krishna, R. Separating Mixtures by Exploiting Molecular Packing Effects in Microporous Materials. *Phys. Chem. Chem. Phys.* **2015**, *17*, 39−59.
(19) Jorgensen, W.; Maxwell, D.; Tirado-Rives, J. Development and Testing of the OPLS All-Atom Force Field on Conformational Energetics and Properties of Organic Liquids. *J. Am. Chem. Soc.* **1996**, *118*, 11225−11236.
(20) Rohrbaugh, R.; Jurs, P. Description of Molecular Shape Applied in Studies of Structure/Activity and Structure/Property Relationships. *Anal. Chim. Acta* **1987**, *199*, 99−109.
(21) *Materials Studio*; Accelrys Software Inc.: San Diego, 2001−2007; http://accelrys.com/products/materials-studio/index.html.
(22) Siu, S. W. I.; Pluhackova, K.; Bockmann, R. A. Optimization of the OPLS-AA Force Field for Long Hydrocarbons. *J. Chem. Theory Comput.* **2012**, *8*, 1459−1470.
(23) Kresse, G.; Hafner, J. Ab initio molecular dynamics for liquid metals. *Phys. Rev. B* **1993**, *47*, 558.
(24) Kresse, G.; Furthmüller, J. Efficient Iterative Schemes for Ab Initio Total-Energy Calculations Using a Plane-Wave Basis Set. *Phys. Rev. B* **1996**, *54*, 11169.
(25) Perdew, J. P.; Burke, K.; Ernzerhof, M. Generalized Gradient Approximation Made Simple. *Phys. Rev. Lett.* **1996**, *77*, 3865.
(26) Perdew, J. P.; Burke, K.; Ernzerhof, M. Erratum: Generalized Gradient Approximation Made Simple. *Phys. Rev. Lett.* **1997**, *78*, 1396.
(27) Grimme, S. Semiempirical GGA-Type Density Functional Constructed with a Long-Range Dispersion Correction. *J. Comput. Chem.* **2006**, *27*, 1787−1799.
(28) Mayo, S.; Olafson, B.; Goddard, W. DREIDING - A Generic Force-field for Molecular Simulations. *J. Phys. Chem.* **1990**, *94*, 8897−8909.
(29) Rappé, A.; Casewit, C.; Colwell, K.; Goddard, W.; Skiff, W. UFF, A Full Periodic-table Force-Field for Molecular Mechanics and Molecular-Dynamics Simulations. *J. Am. Chem. Soc.* **1992**, *114*, 10024−10035.
(30) Bai, P.; Tsapatsis, M.; Siepmann, J. I. TraPPE-zeo: Transferable Potentials for Phase Equilibria Force Field for All-Silica Zeolites. *J. Phys. Chem. C* **2013**, *117*, 24375−24387.
(31) Campana, C.; Mussard, B.; Woo, T. Electrostatic Potential Derived Atomic Charges for Periodic Systems Using a Modified Error Functional. *J. Chem. Theory Comput.* **2009**, *5*, 2866−2878.
(32) Watanabe, T.; Manz, T.; Sholl, D. Accurate Treatment of Electrostatics during Molecular Adsorption in Nanoporous Crystals without Assigning Point Charges to Framework Atoms. *J. Phys. Chem. C* **2011**, *115*, 4824−4836.
(33) Torres-Knoop, A.; Balaji, S. P.; Vlugt, T.; Dubbeldam, D. A Comparison of Advanced Monte Carlo Methods for Open Systems: CFCMC vs CBMC. *J. Chem. Theory Comput.* **2014**, *10*, 942−952.
(34) Siepmann, J. A. Method for the Direct Calculation of Chemical-Potentials for Dense Chain Systems. *Mol. Phys.* **1990**, *70*, 1145−1158.
(35) Siepmann, J.; Frenkel, D. Configurational Bias Monte-Carlo - A New Sampling Scheme for Flexible Chains. *Mol. Phys.* **1992**, *75*, 59−70.
(36) Frenkel, D.; Mooij, G.; Smit, B. Novel Scheme to Study Structural and Thermal-properties of Continuously Deformable Molecules. *J. Phys.: Condens. Matter* **1992**, *4*, 3053−3076.
(37) Shi, W.; Maginn, E. Continuous Fractional Component Monte Carlo: An Adaptive Biasing Method for Open System Atomistic Simulations. *J. Chem. Theory Comput.* **2007**, *3*, 1451−1463.
(38) Krishna, R. The Maxwell-Stefan Description of Mixture Diffusion in Nanoporous Crystalline Materials. *Microporous Mesoporous Mater.* **2014**, *185*, 30−50.
(39) Krishna, R.; Long, J. Screening Metal-organic Frameworks by Analysis of Transient Breakthrough of Gas Mixtures in a Fixed Bed Adsorber. *J. Phys. Chem. C* **2011**, *115*, 12941−12950.
(40) van Koningsveld, H.; F. Tuinstra, H. v. B.; Jansen, J. C. The Location of p-Xylene in a Single Crystal of Zeolite H-ZSM-5 with a New Sorbate-Induced, Orthorombic Framework Symmetry. *Acta Crystallogr.* **1989**, *B45*, 423−431.
(41) Galli, E. Crystal Structure Refinement of Mazzite. *Rend. Soc. Ital. Mineral. Petrol.* **1975**, *31*, 599−612.
(42) Qiu, S.; Pang, W.; Kessler, H.; Guth, J. Synthesis and Structure of the $[AlPO_4]_{12}Pr_4NF$ Molecular Sieve with AFI Structure. *Zeolites* **1989**, *9*, 440−444.

DOI: 10.1021/acs.langmuir.5b00363
Langmuir 2015, 31, 3771−3778

(43) Wessels, T.; Baerlocher, C.; McCusker, L.; Creyghton, E. An Ordered Form of the extra-large-pore zeolite UTD-1: Synthesis and Structure Analysis from Powder Diffraction Data. *J. Am. Chem. Soc.* **1999**, *121*, 6242−6247.
(44) Serre, C.; Millange, F.; Thouvenot, C.; Nogues, M.; Marsolier, G.; Louer, D.; Ferey, G. Very Large Breathing Effect in the First Nanoporous Chromium(III)-based Solids: MIL-53 or $Cr^{III}(OH)\cdot\{O_2C-C_6H_4-CO_2\}\cdot\{HO_2C-C_6H_4)-CO_2H\}_x\cdot H_2O_y$. *J. Am. Chem. Soc.* **2002**, *124*, 13519−13526.
(45) Barthelet, K.; Marrot, J.; Riou, D.; Ferey, G. A Breathing Hybrid Organic-Inorganic Solid with very Large Pores and High Magnetic Characteristics. *Ang. Chem., Int. Ed.* **2002**, *41*, 281−284.
(46) He, C.-T.; Tian, J.-Y.; Liu, S.-Y.; Ouyang, G.; Zhang, J.-P.; Chen, X.-M. A Porous Coordination Framework for Highly Sensitive and Selective Solid-Phase Microextraction of Non-polar Volatile Organic Compounds. *Chem. Sci.* **2013**, *4*, 351−356.
(47) Fang, Z.; Zheng, S.; Tan, J.; Cai, S.; Fan, J.; Yan, X.; Zhang, W. Tubular Metal-Organic Framework-based Capillary Gas Chromatography Column for Separation of Alkanes and Aromatic Positional Isomers. *J. Chromatogr. A* **2013**, 132−138.

DOI: 10.1021/acs.langmuir.5b00363
Langmuir 2015, 31, 3771−3778

Supporting Information to accompany:

Entropic Separation of Styrene/Ethylbenzene Mixtures by Exploitation of Subtle Differences in Molecular Configurations in Ordered Crystalline Nanoporous Adsorbents

Ariana Torres-Knoop[1], Jurn Heinen, Rajamani Krishna, and David Dubbeldam
Van 't Hoff Institute for Molecular Sciences, University of Amsterdam,
Science Park 904, 1098XH, Amsterdam, The Netherlands

March 2, 2015

[1]email: A.TorresKnoop@uva.nl

1 Adsorption isotherms

To compute the adsorption isotherms we performed Monte Carlo simulations in the grand-canonical ensemble (or μ, V, T ensemble). In this ensemble, the temperature T, the volume V, and the chemical potential μ are fixed. The Metropolis algorithm is implemented in the same way as for NVT ensemble, but in this case also the number of adsorbates is allowed to change by having an insertion and a deletion move. The number of adsorbates will fluctuate until equilibrium conditions are reached: the temperature and chemical potential of the gas inside and outside the adsorbent are equal. The imposed chemical potential is related to the fugacity f by

$$\beta\mu = \beta\mu^0_{\mathrm{id}} + \ln(\beta f), \tag{1.1}$$

where μ^0_{id} is the reference chemical potential and β the inverse of temperature.

Because in confined systems the fraction of successful insertions and deletions is very low, reaching equilibrium with conventional Monte Carlo methods can be very time consuming. In this study we use the Configurational Bias Continuous Fractional Monte Carlo (CB/CFCMC) [1] method to enhance the success rate of insertions and deletions. The method is a combination of the Configurational Bias Monte Carlo (CBMC)[2, 3, 4], where molecular growth is biased towards favorable configurations and Continuous Fractional Component Monte Carlo (CFCMC) [5] in which molecules are gradually inserted or deleted by scaling their intermolecular interactions with the surroundings using a parameter λ. In this method, new molecules are inserted and old chains are removed using configurational biasing at constant λ values and λ is changed by using $\lambda(n) = \lambda(o) + \epsilon$, where ϵ is chosen uniformly between $-\Delta\lambda^{\max}$ and $+\Delta\lambda^{\max}$ and adjusted to achieve approximately 50% acceptance. Because many systems show behavior where λ-changes are difficult [5, 6, 7], an additional bias η on λ can be used which is afterwards removed by the acceptance rules. When $\lambda = 0$ or $\lambda = 0 = 1$ the algorithm reduces to conventional CBMC for insertion and deletion, respectively. We have shown in previous work[1] that the results obtain with this method do not differ from CBMC calculations but the efficiency is higher. The acceptance rules for insertion and deletion are given by:

- Insertion move, $\lambda_n = 1 + \epsilon$
  A new fractional molecule with $\lambda_n = \epsilon$ is grown at a random position using CBMC giving $W(n)$.

$$\mathrm{acc}\,(\mathrm{o} \to \mathrm{n}) = \min\left(1, \frac{f\beta V}{N+1}\frac{W(n)}{\langle W^{\mathrm{IG}}\rangle}\exp[-\beta\Delta U]\exp[\eta(\lambda(n)) - \eta(\lambda(o))]\right) \tag{1.2}$$

- Deletion move, $\lambda_n = -\epsilon$
  The existing fractional particle is retraced using CBMC with $\lambda = \lambda_o$ giving W(o) and the fractional molecule is subsequently removed.

$$\mathrm{acc}\,(\mathrm{o} \to \mathrm{n}) = \min\left(1, \frac{N}{f\beta V}\frac{\langle W^{\mathrm{IG}}\rangle}{W(o)}\exp[-\beta\Delta U]\exp[\eta(\lambda(n)) - \eta(\lambda(o))]\right) \tag{1.3}$$

Together with insertion and deletion moves, several types of Monte Carlo moves are employed during a simulation to thermalize the system:

- Displacement move
  A molecule is selected at random and given a random displacement. The maximum displacement is taken such that 50% of the moves is accepted. The acceptance rule is

$$\mathrm{acc}\left(\mathrm{o} \rightarrow \mathrm{n}\right) = \min\left(1, e^{-\beta\left(U^{\mathrm{n}} - U^{\mathrm{o}}\right)}\right). \tag{1.4}$$

  Note that the energy of the new configuration U^{n} and the energy of the old configuration U^{o} only differ in the external energy.

- Rotation move
  A molecule is selected at random and given a random rotation. The center of the rotation is the center of mass. The maximum rotation angle is selected such that 50% of the moves are accepted. The acceptance rule is given by Eq. 1.4. Again, the energy of the new configuration U^{n} and the energy of the old configuration U^{o} only differ in the external energy.

- Identity change move (mixtures)
  The identity-change trial move [8] is called semi-grand ensemble, but it can also be seen as a special case of the Gibbs ensemble. One of the components is selected at random and an attempt is made to change its identity. The acceptance rule is given by [9]

$$\mathrm{acc}\left(\mathrm{A} \rightarrow \mathrm{B}\right) = \min\left(1, \frac{W^{\mathrm{new}} f_B \left\langle W_A^{\mathrm{IG}} \right\rangle N_A}{W^{\mathrm{old}} f_A \left\langle W_B^{\mathrm{IG}} \right\rangle \left(N_B + 1\right)}\right), \tag{1.5}$$

  where f_A and f_B are the fugacities of components A and B, and N_A and N_B are the number of particles.

Simulations are performed in cycles. The number of cycles needed for equilibration depends on the number of molecules. We define a cycle to consists of smaller steps proportional to the number number of molecules with 20 as the minimum.

$$N_{\mathrm{cycles}} = \max\left(20, N\right) \times N_{\mathrm{steps}}. \tag{1.6}$$

In each step one Monte Carlo move is performed. For the isotherms we used at least 500000 initialization cycles, while 500000 cycles are used to compute the isotherms. The error bars in the isotherms are computed by dividing the simulations results up into five blocks. The error is computed from the standard deviation of the five blocks and corresponds to the 95% confidence interval.

2
Case Studies

2.1 MFI-para: size exclusion

2.1.1 Snapshots

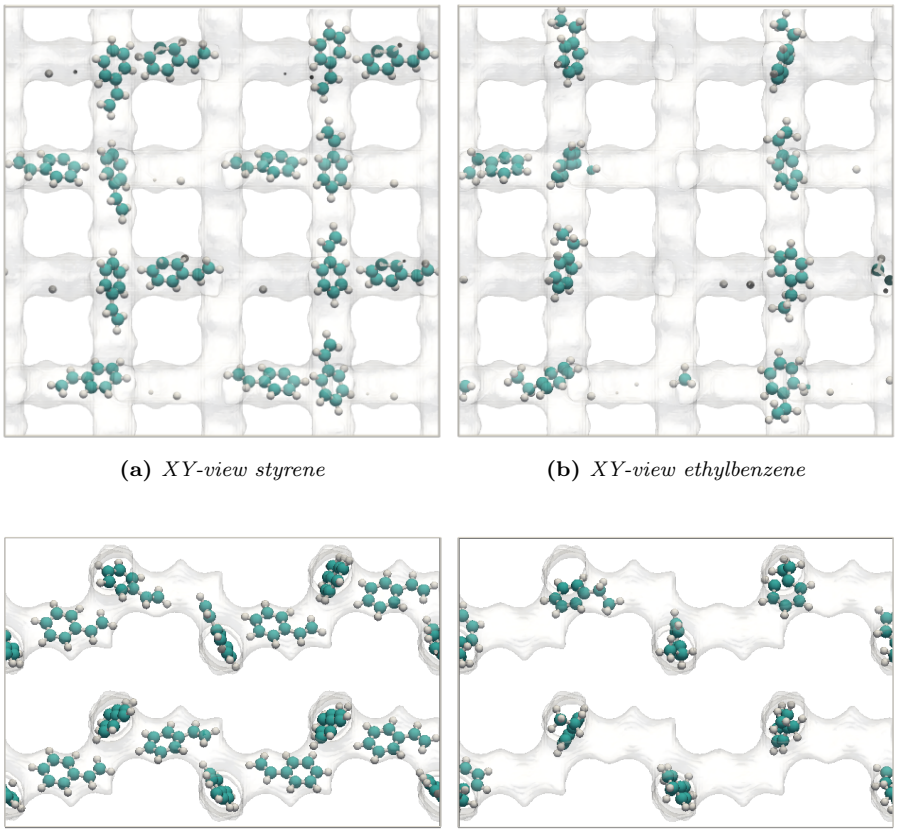

(a) *XY-view styrene* **(b)** *XY-view ethylbenzene*

(c) *XZ-view styrene* **(d)** *XZ-view ethylbenzene*

Figure S1: *Snapshots of styrene and ethylbenzene in MFI-para at 433K and 1e9Pa. Styrene can be adsorbed in the straight and the zig-zag channels but ethylbenzene positions in the zig-zag channels are hindered by the ones in the intersections The size exclusion effect in the zig-zag channels causes a significant difference in the saturation capacities of both molecules. MFI-para is a styrene selective structure at saturation capacity. Color code: carbon (cyan), hydrogen (white).*

2.1.2 Langmuir-Freundlich parameters

	site A			site B		
	$q_{i,A,\text{sat}}$ [mol kg^{-1}]	$b_{i,A}$ [Pa$^{-\nu_{i,A}}$]	$\nu_{i,A}$ [-]	$q_{i,B,\text{sat}}$ [mol kg^{-1}]	$b_{i,B}$ [Pa$^{-\nu_{i,B}}$]	$\nu_{i,B}$ [-]
styrene	0.61	1.41×10^{-5}	1.1	0.6	1.61×10^{-7}	1.03
ethylbenzene	0.14	4.95×10^{-6}	1.05	0.57	1.96×10^{-7}	1.15

Table S1: *Dual-site Langmuir-Freundlich parameters for pure component styrene and ethylbenzene isotherms at 433K in MFI-para.*

2.1.3 Adsorption isotherms

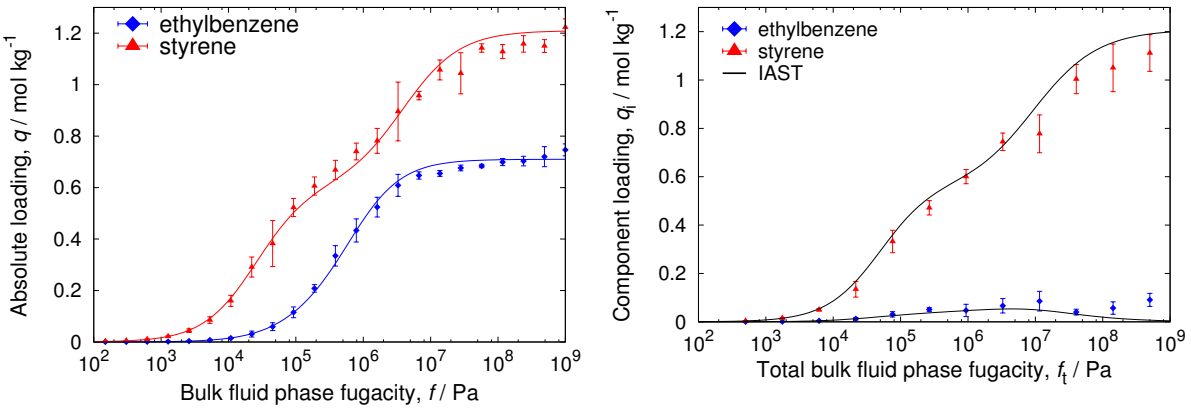

Figure S2: *Simulated isotherms of styrene and ethylbenzene in MFI-para at 433K. (a) Pure component isotherms (lines are dual-site Langmuir-Freundlich fits of the pure components, points are the pure component isotherms from CB/CFCMC simulations) (b) mixture component isotherms for an equimolar mixture.The IAST results are in good agreement with the mixture isotherms.*

2.1.4 Breakthrough simulations

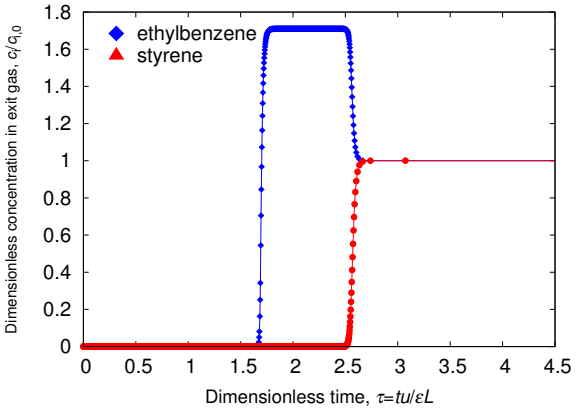

Figure S3: *Simulated step-type breakthrough curves of an equimolar mixture of styrene and ethylbenzene in MFI-para at 433K and 1e6 Pa total fugacity. Video animations of the breakthrough behavior as a function of time are provided as Supplementary information.*

2.2 AFI: face-to-face stacking

2.2.1 Snapshots

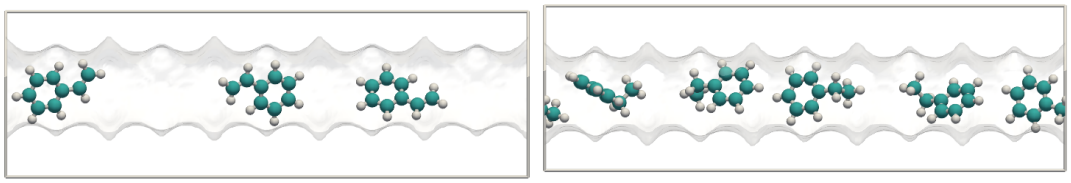

(a) *1e4 Pa*

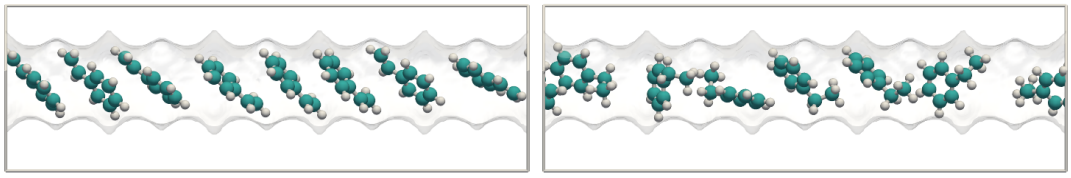

(b) *1e9 Pa*

Figure S4: *Snapshots of styrene (left) and ethylbenzene (right) in AFI zeolite at 433K and 1e4 Pa (top) and 1e9 Pa (bottom). At low loadings, molecules are preferentially adsorbed flat on the walls (parallel to the channel axis) to enhance their interactions. Ethylbenzene has stronger interactions with the framework under these conditions. At saturation loadings styrene undergoes a molecular reorientation into a face-to-face configuration. This reorientation reduces styrene's footprint in the channels allowing for more molecules to be adsorbed and a higher saturation capacity to be obtained. Ethylbenzene size does not allow for this reorientation to be completed. Color code: carbon (cyan), hydrogen (white).*

2.2.2 Langmuir-Freundlich parameters

	site A			site B		
	$q_{i,A,\text{sat}}$ [mol kg^{-1}]	$b_{i,A}$ [Pa$^{-\nu_{i,A}}$]	$\nu_{i,A}$ [-]	$q_{i,B,\text{sat}}$ [mol kg^{-1}]	$b_{i,B}$ [Pa$^{-\nu_{i,B}}$]	$\nu_{i,B}$ [-]
styrene	0.3	8.1×10^{-8}	1	0.8	1.23×10^{-4}	1
ethylbenzene	0.3	8.44×10^{-6}	0.74	0.67	1.45×10^{-4}	1.1

Table S2: *Dual-site Langmuir-Freundlich parameters for pure component styrene and ethylbenzene at 433K in AFI.*

2.2.3 Adsorption isotherms

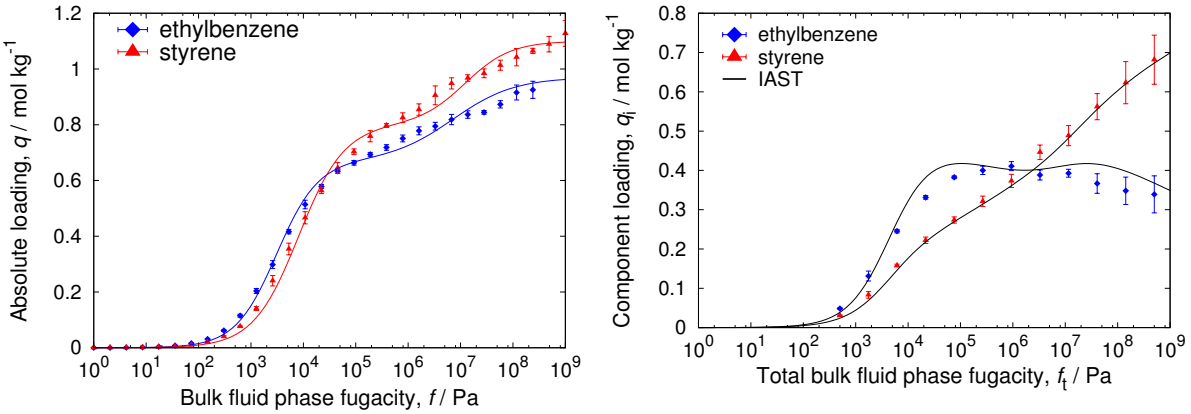

(a) **(b)**

Figure S5: *Simulated isotherm of styrene and ethylbenzene in AFI zeolite at 433K. (a) Pure component isotherms (lines are dual-site Langmuir-Freundlich fits of the pure components, points are the pure component isotherms from CB/CFCMC simulations) (b) mixture component isotherms for an equimolar mixture. The IAST results are in good agreement with the mixture isotherms*

2.2.4 Breakthrough simulations

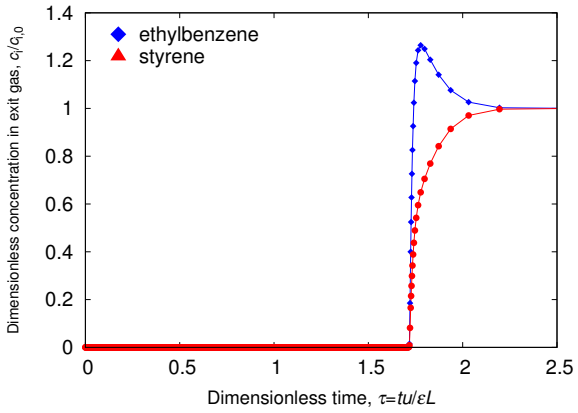

Figure S6: *Simulated step-type breakthrough of styrene and ethylbenzene in AFI at 433K and 1e6 Pa total fugacity. Video animations of the breakthrough behavior as a function of time are provided as Supplementary information.*

2.3 MAZ: face-to-face stacking

2.3.1 Snapshots

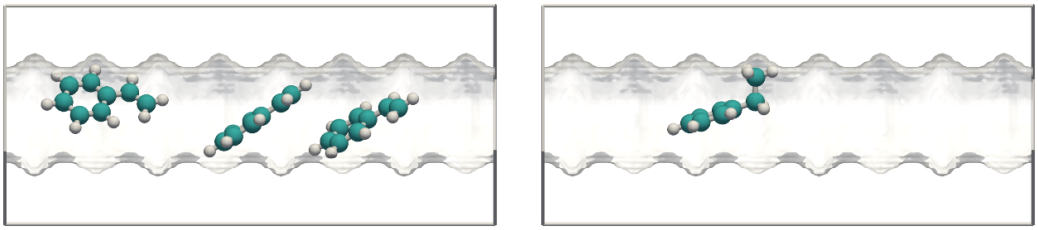

(a) *1e4 Pa*

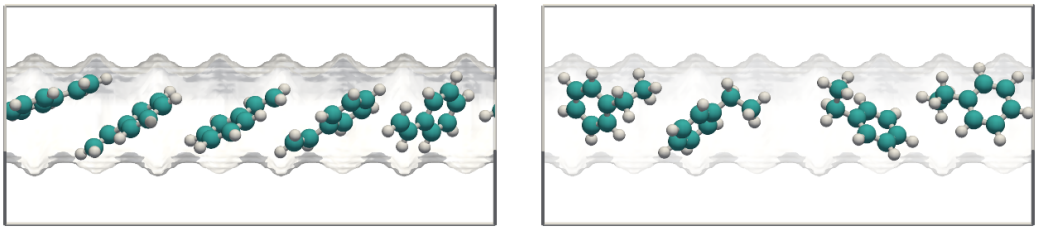

(b) *1e9 Pa*

Figure S7: *Snapshots of styrene (left) and ethylbenzene (right) in MAZ zeolite at 1e4 Pa (top) and 1e9 Pa (bottom) and 433K. MAZ zeolite has slightly smaller channels than AFI. The size of the channel determines how tilted the molecules have to be in a face-to-face stacking configuration and therefore it determines the molecule's footprint in the channel after reorientation. At low loadings, styrene adsorbs parallel to the channel axis, but MAZ channel's dimensions still make the reorientation into a face-to-face stacking configuration at high loadings favorable. Styrene footprint in the channels is reduced and a higher saturation capacity is obtain. For ethylbenzene, because of the non-planar ethyl group, a reorientation into face-to-face stacking does not reduce significantly the footprint of the molecule in the channels and therefore is not favorable. At saturation conditions MAZ is a styrene selective structure.*

2.3.2 Langmuir-Freundlich parameters

	site A			site B		
	$q_{i,A,\text{sat}}$ [mol kg^{-1}]	$b_{i,A}$ [Pa$^{-\nu_{i,A}}$]	$\nu_{i,A}$ [-]	$q_{i,B,\text{sat}}$ [mol kg^{-1}]	$b_{i,B}$ [Pa$^{-\nu_{i,B}}$]	$\nu_{i,B}$ [-]
styrene	0.2	6.8×10^{-6}	0.8	0.4	1.22×10^{-4}	1.05
ethylbenzene	0.12	3.89×10^{-6}	0.67	0.42	1.72×10^{-4}	1.02

Table S3: *Dual-site Langmuir-Freundlich parameters for pure component styrene and ethylbenzene at 433K in MAZ.*

2.3.3 Adsorption isotherms

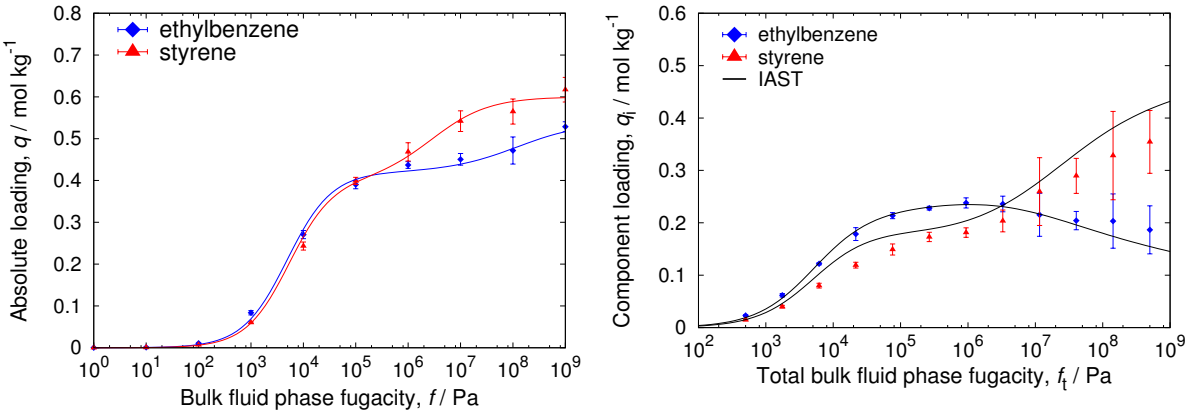

(a) **(b)**

Figure S8: *Simulated isotherms of styrene and ethylbenzene in MAZ at 433K. (a) Pure component isotherms (lines are dual-site Langmuir-Freundlich fits of the pure components, points are the pure component isotherms from CB/CFCMC simulations)(b) mixture component isotherms for an equimolar mixture. The IAST results are in good agreement with the mixture isotherms*

2.3.4 Breakthrough simulations

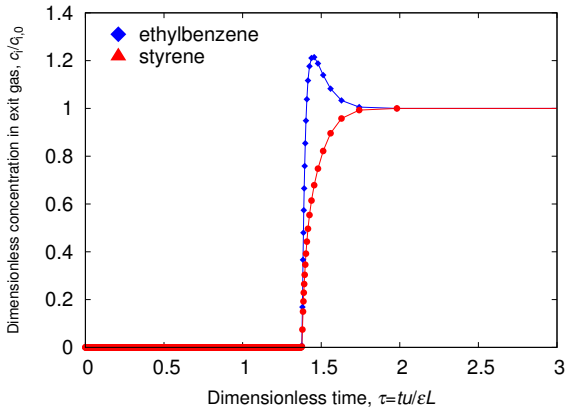

Figure S9: *Simulated step-type breakthrough of styrene and ethylbenzene in AFI at 433K and 1e6 total fugacity. Video animations of the breakthrough behavior as a function of time are provided as Supplementary information.*

2.4 DON: styrene commensurate stacking and ethylbenzene face-to-face stacking

2.4.1 Snapshots

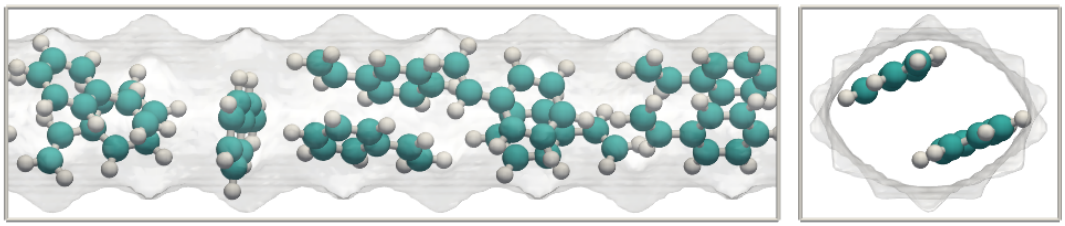

(a) *Styrene*

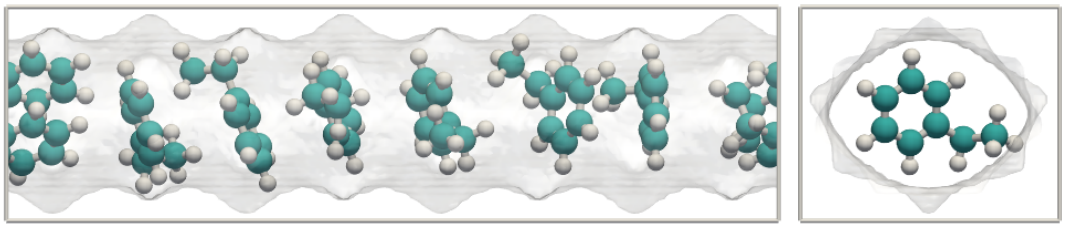

(b) *Ethylbenzene*

Figure S10: *Snapshots of styrene (top) and ethylbenzene (bottom) in DON zeolite at 1e9Pa and 433K. DON zeolite has larger channels than AFI and MAZ. Because of that, ethylbenzene can also undergo a reorientation into face-to-face stacking configuration that reduces its footprint in the channel. The channel dimensions however are also large enough for styrene to have commensurate stacking. Commensurate stacking allows styrene to obtain a higher saturation capacity than the one obtained by ethylbenzene in a face-to-face stacking configuration. Color code: carbon (cyan), hydrogen (white).*

2.4.2 Langmuir-Freundlich parameters

	site A			site B		
	$q_{i,A,\text{sat}}$ [mol kg^{-1}]	$b_{i,A}$ [Pa$^{-\nu_{i,A}}$]	$\nu_{i,A}$ [-]	$q_{i,B,\text{sat}}$ [mol kg^{-1}]	$b_{i,B}$ [Pa$^{-\nu_{i,B}}$]	$\nu_{i,B}$ [-]
styrene	0.2	8.75×10^{-7}	0.9	0.9	3.54×10^{-5}	1.1
ethylbenzene	0.3	3.64×10^{-6}	0.8	0.75	6.61×10^{-5}	1.1

Table S4: *Dual-site Langmuir-Freundlich parameters for pure component styrene and ethylbenzene at 433K in DON.*

2.4.3 Adsorption isotherms

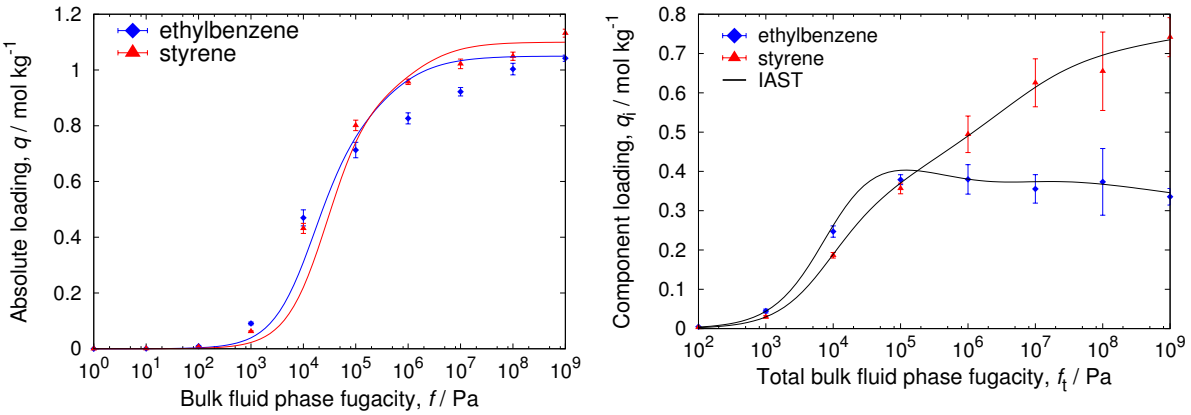

(a) (b)

Figure S11: *Simulated isotherms of styrene and ethylbenzene in DON zeolite at 433K. (a) Pure component isotherms (lines are dual-site Langmuir-Freundlich fits of the pure components, points are the pure component isotherms from CB/CFCMC simulations) (b) mixture component isotherms for an equimolar mixture. The IAST results are in good agreement with the mixture isotherms*

2.4.4 Breakthrough simulations

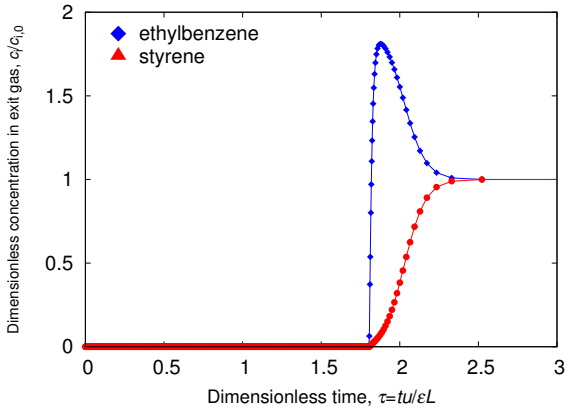

Figure S12: *Simulated step-type breakthrough of styrene and ethylbenzene in DON at 433K and 1e6 Pa total fugacity. Video animations of the breakthrough behavior as a function of time are provided as Supplementary information.*

2.5 MIL-53: styrene commensurate stacking and ethylbenzene face-to-face stacking

2.5.1 Snapshots

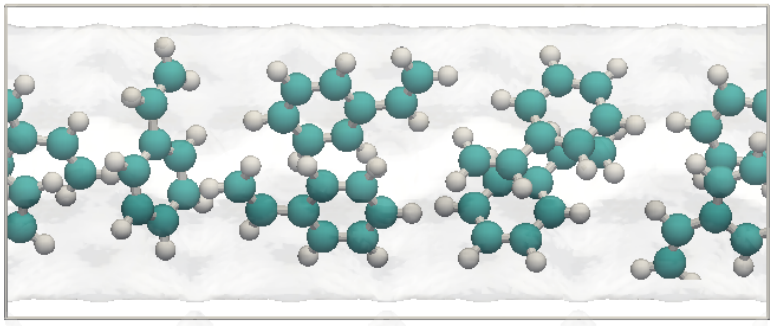

(a) *XZ-view styrene*

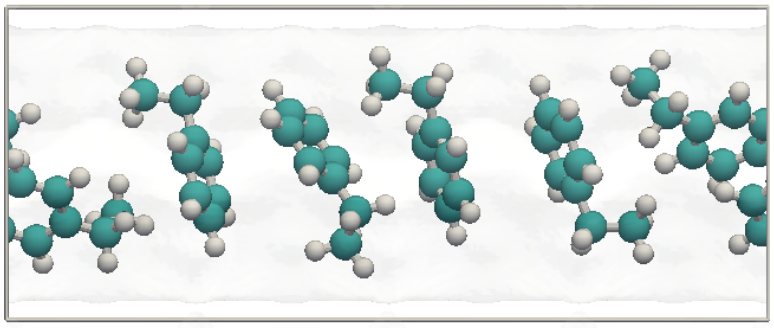

(b) *XZ-view ethylbenzene*

Figure S13: *Snapshots of styrene (top) and ethylbenzene (bottom) in MIL-53 at 1e9 Pa and 433K. Ethylbenzene has a face-to-face stacking configuration while styrene has commensurate stacking. Color code: carbon (cyan), hydrogen (white).*

2.5.2 Langmuir-Freundlich parameters

	site A			site B		
	$q_{i,A,\text{sat}}$ [mol kg^{-1}]	$b_{i,A}$ [Pa$^{-\nu_{i,A}}$]	$\nu_{i,A}$ [-]	$q_{i,B,\text{sat}}$ [mol kg^{-1}]	$b_{i,B}$ [Pa$^{-\nu_{i,B}}$]	$\nu_{i,B}$ [-]
styrene	1.33	7.15×10^{-4}	0.66	2	3.74×10^{-3}	1.07
ethylbenzene	0.73	5.41×10^{-5}	0.73	2.2	6.6×10^{-3}	1

Table S5: *Dual-site Langmuir-Freundlich parameters for pure component styrene and ethylbenzene at 433K in MIL-53.*

2.5.3 Adsorption isotherms

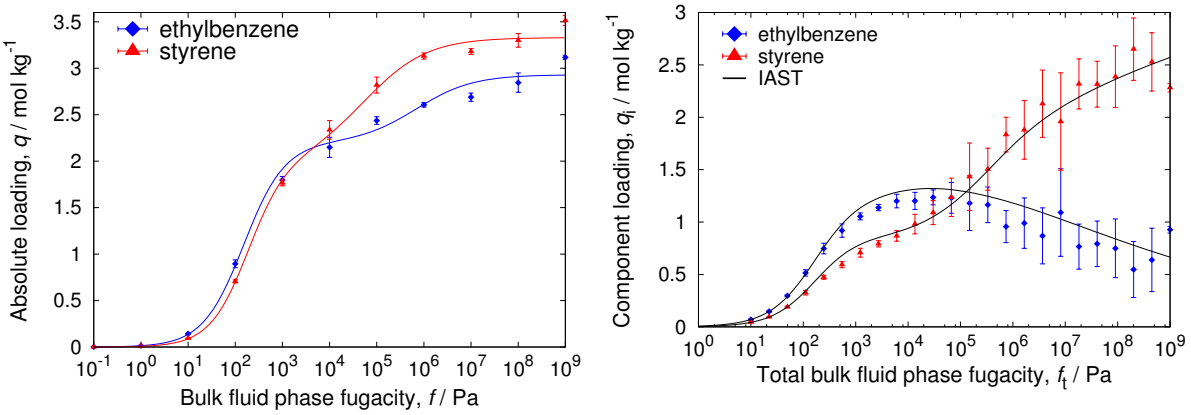

(a) **(b)**

Figure S14: *Simulated isotherms of styrene and ethylbenzene in MIL-53 at 433K. (a) Pure component isotherms (lines are dual-site Langmuir-Freundlich fits of the pure components, points are the pure component isotherms from CB/CFCMC simulations) (b) mixture component isotherms for an equimolar mixture. The IAST results are in good agreement with the mixture isotherms*

2.5.4 Breakthrough simulations

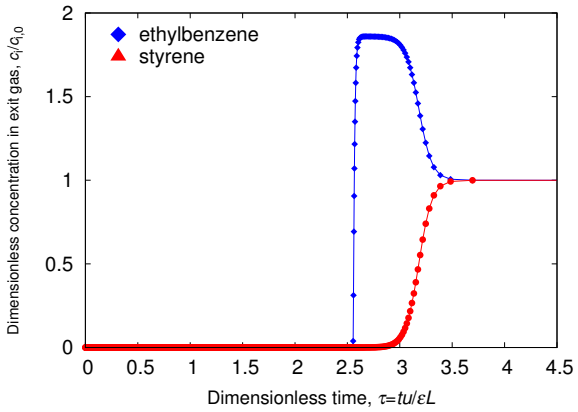

Figure S15: *Simulated step-type breakthrough of styrene and ethylbenzene in MIL-53 at 433K and 1e6 Pa total fugacity. Video animations of the breakthrough behavior as a function of time are provided as Supplementary information.*

2.6 MIL-47: commensurate stacking

2.6.1 Snapshots

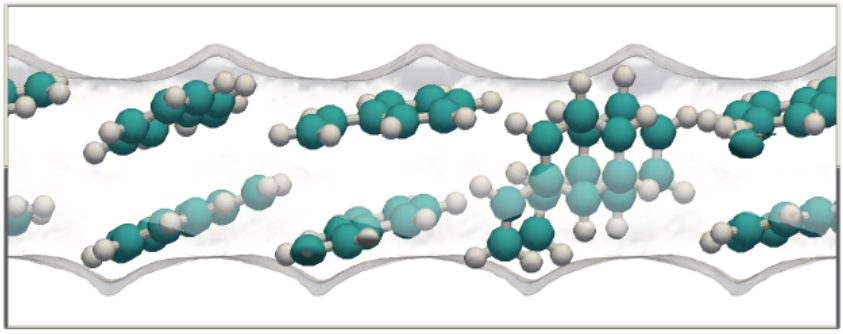

(a) *Styrene*

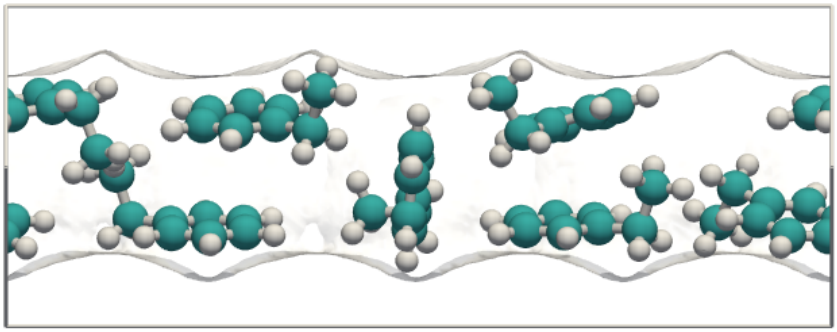

(b) *Ethylbenzene*

Figure S16: *Snapshots of styrene (top) and ethylbenzene (bottom) in MIL-47 at 1e9 Pa and 433K. Both, ethylbenzene and styrene molecules have commensurate stacking. However the "length" of the packing of styrene in the channels is smaller. This allows styrene to obtain a higher saturation capacity than ethylbenzene. MIL-47 is a styrene selective structure. Color code: carbon (cyan), hydrogen (white).*

2.6.2 Langmuir-Freundlich parameters

	site A			site B		
	$q_{i,A,\text{sat}}$ [mol kg^{-1}]	$b_{i,A}$ [Pa$^{-\nu_{i,A}}$]	$\nu_{i,A}$ [-]	$q_{i,B,\text{sat}}$ [mol kg^{-1}]	$b_{i,B}$ [Pa$^{-\nu_{i,B}}$]	$\nu_{i,B}$ [-]
styrene	1.4	4.11×10^{-4}	0.67	2.9	1.89×10^{-3}	1.1
ethylbenzene	1.2	3.45×10^{-3}	0.44	2.3	3.73×10^{-3}	1.1

Table S6: *Dual-site Langmuir-Freundlich parameters for pure component xylene isomers at 433 K in MIL-47.*

2.6.3 Adsorption isotherms

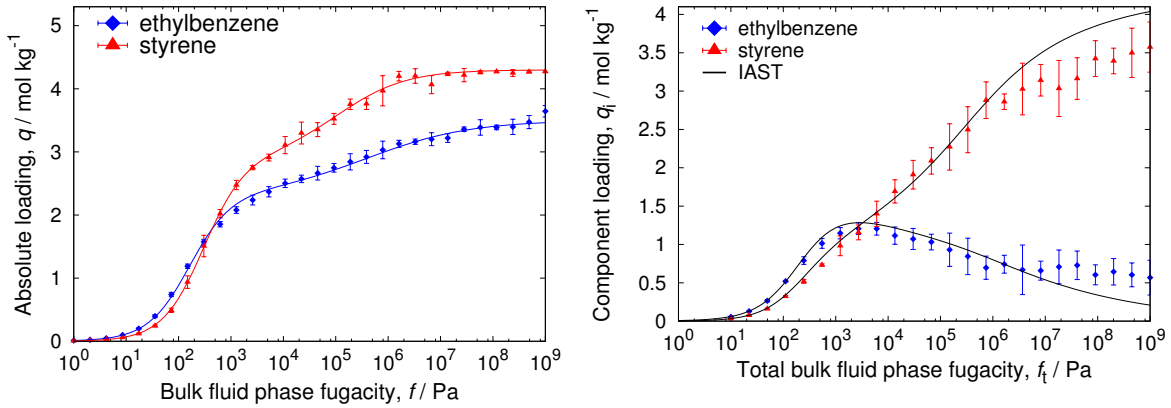

(a) **(b)**

Figure S17: *Simulated isotherms of styrene and ethylbenzene in MIL-47 at 433K. (a) Pure component isotherms (lines are dual-site Langmuir-Freundlich fits of the pure components, points are the pure component isotherms from CB/CFCMC simulations) and mixture component isotherms for an equimolar mixture. The IAST results are in good agreement with the mixture isotherms*

2.6.4 Breakthrough simulations

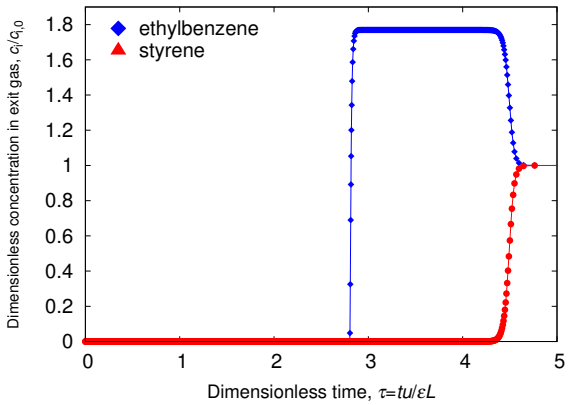

Figure S18: *Simulated step-type breakthrough of styrene and ethylbenzene in MIL-47 at 433K and 1e6 Pa total fugacity. Video animations of the breakthrough behavior as a function of time are provided as Supplementary information.*

2.7 MAF-X8: commensurate stacking

2.7.1 Snapshots

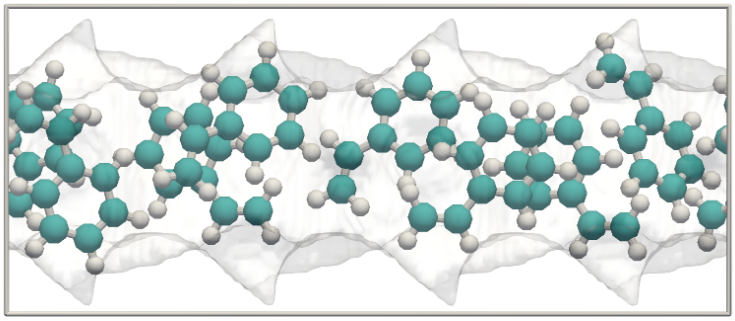

(a) *XY-view styrene*

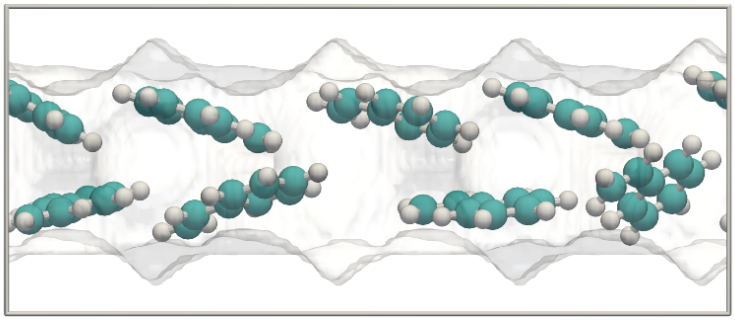

(b) *YZ-view styrene*

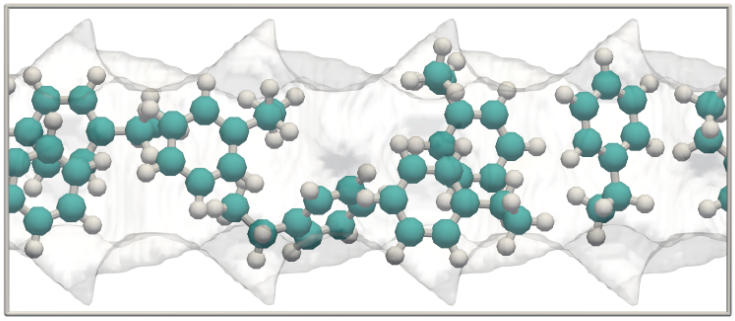

(c) *XY-view ethylbenzene*

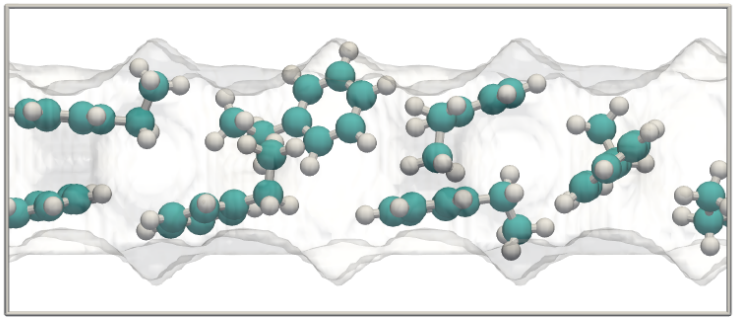

(d) *YZ-view ethylbenzene*

Figure S19: *Snapshots of styrene (top) and ethylbenzene (bottom) in MAF-X8 at 1e9 Pa and 433K. Both styrene and ethylbenzene have commensurate stacking. Color code: carbon (cyan), hydrogen (white).*

2.7.2 Adsorption isotherms

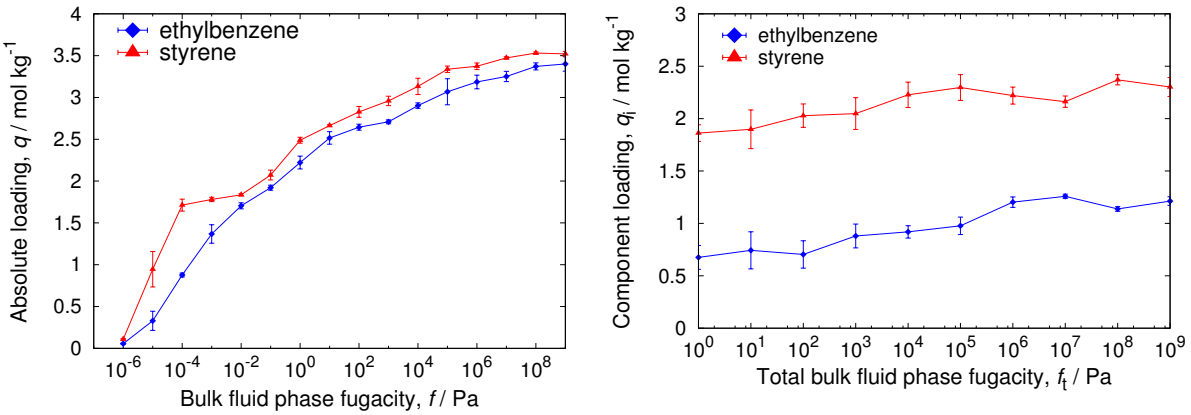

Figure S20: *Simulated isotherms of styrene and ethylbenzene in MAF-X8 at 433K. (a) Pure component isotherms from CB/CFCMC simulations (b) mixture component isotherms for an equimolar mixture.*

2.8 MOF-CJ3: combination of effects

2.8.1 Snapshots

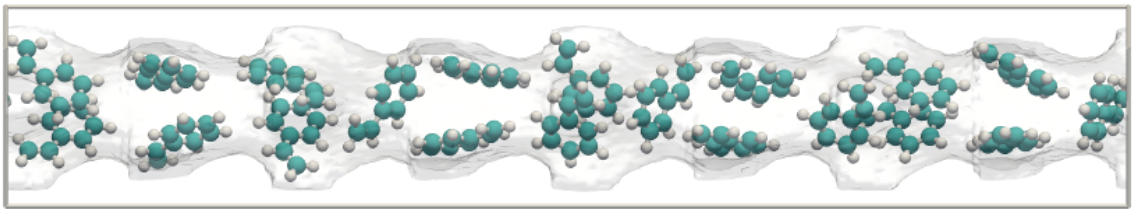

(a) *XZ-view styrene*

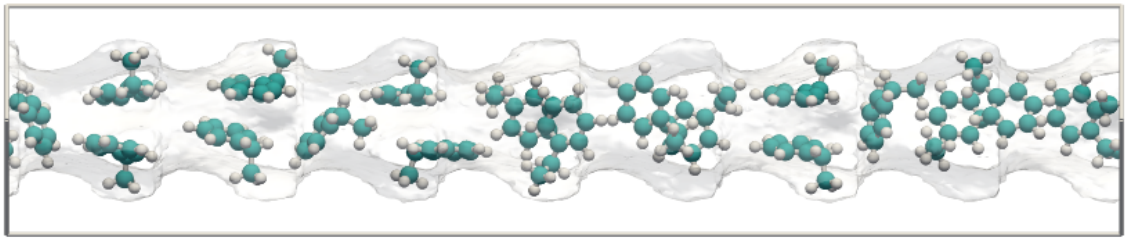

(b) *XZ-view ethylbenzene*

Figure S21: *Snapshots of styrene (top) and ethylbenzene (bottom) in MOF-CJ3 at 1e9 Pa and 433K. Color code: carbon (cyan), hydrogen (white).*

2.8.2 Langmuir-Freundlich parameters

2.8.3 Adsorption isotherms

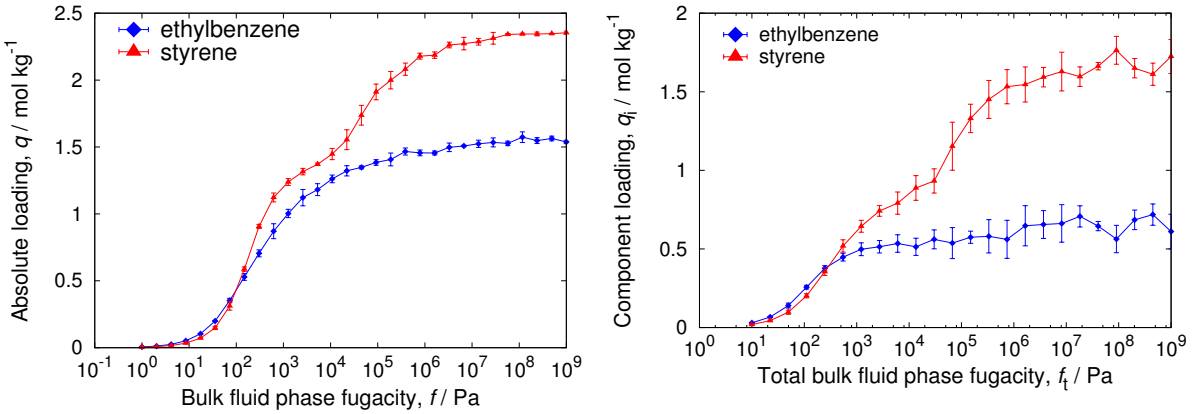

(a) (b)

Figure S22: *Simulated isotherms of styrene and ethylbenzene in MOF-CJ3 at 433K. (a) Pure component isotherms (b) mixture component isotherms for an equimolar mixture.*

2.8.4 Breakthrough simulations

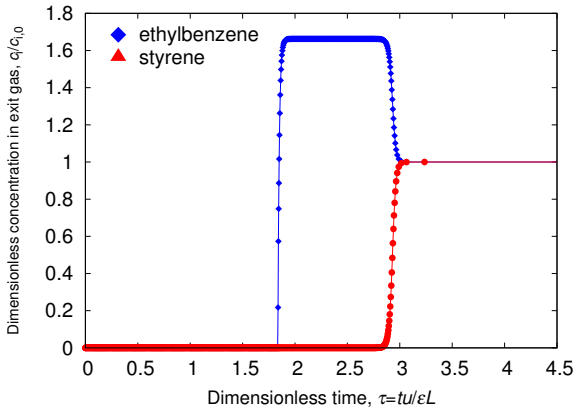

Figure S23: *Simulated step-type breakthrough of styrene and ethylbenzene in MOF-CJ3 at 433K and 1e6 Pa total fugacity. Video animations of the breakthrough behavior as a function of time are provided as Supplementary information.*

2.9 Snapshots MRE

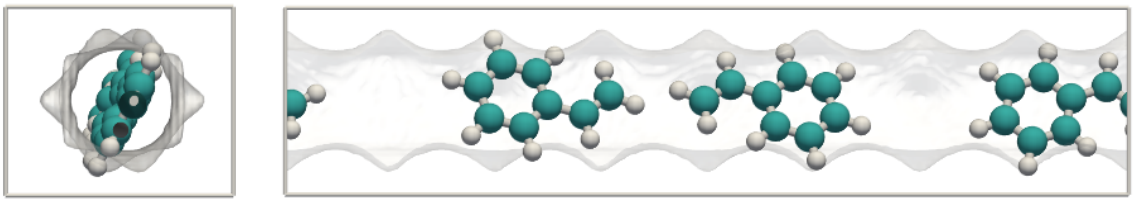

(a) *styrene*

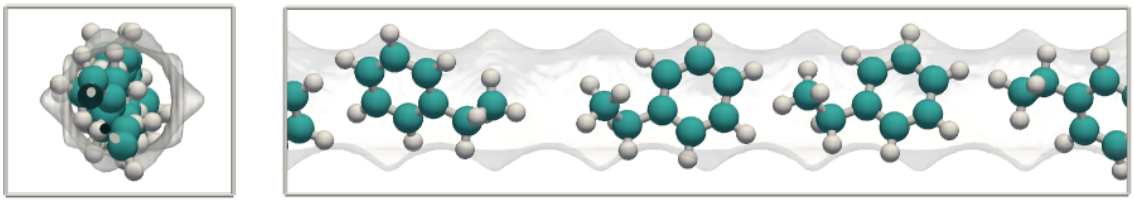

(b) *ethylbenzene*

Figure S24: *Snapshots of styrene and ethylbenzene in MRE zeolite at 433K and 1e9 Pa. The channel dimensions are only large enough for molecules to be adsorb parallel to the channel axis. Because styrene and ethylbenzene main difference is their height (non-planarity of ethyl group) and not the molecule's lengths, their saturation capacity will be very similar. Color code: carbon (cyan), hydrogen (white).*

2.10 Snapshots MTW

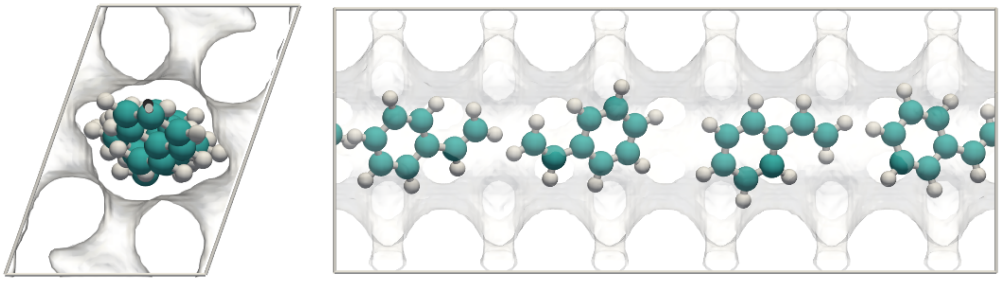

(a) *styrene*

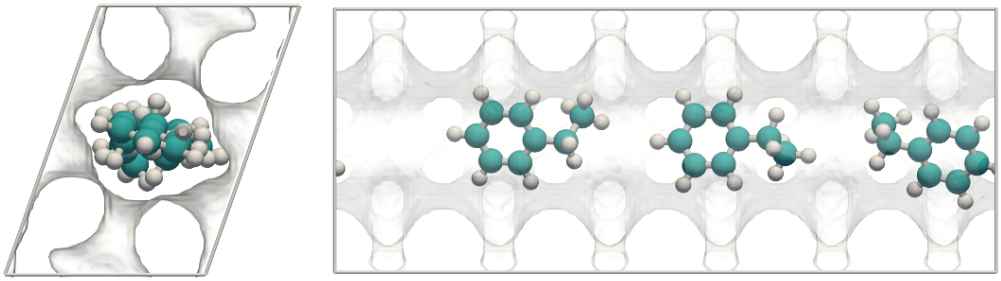

(b) *ethylbenzene*

Figure S25: *Snapshots of styrene and ethylbenzene in MTW zeolite at 433K and 1e9 Pa. As in MRE, because both molecules have a very similar length and they can only adsorb parallel to the channel axis, no mayor difference will be observed in the saturation capacity of these molecules. Color code: carbon (cyan), hydrogen (white).*

2.10.1 Mixture isotherms IRMOF-1, JUC-77, MIL-125, CoBDP

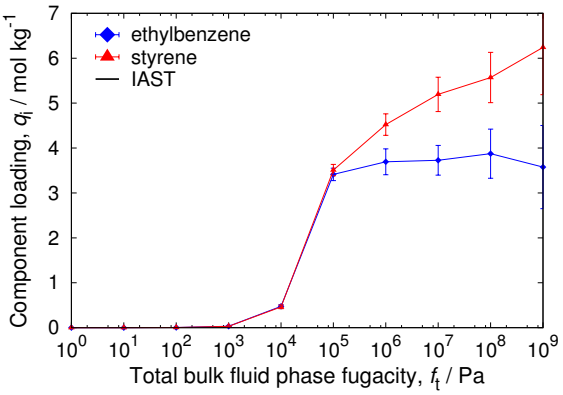

(a)

Figure S26: *Simulated mixture component isotherms in IRMOF-1at 433K.*

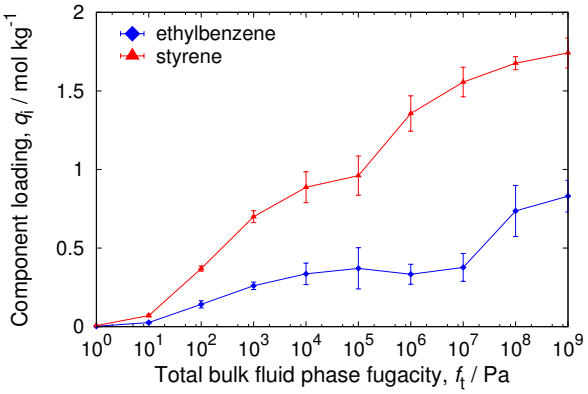

Figure S27: *Simulated mixture component isotherms in JUC-77 at 433K.*

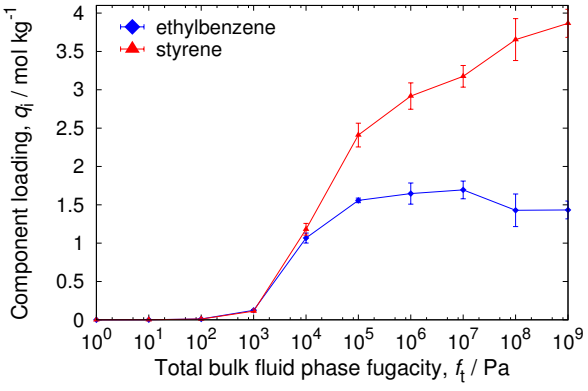

Figure S28: *Simulated mixture component isotherms in MIL-125 at 433K.*

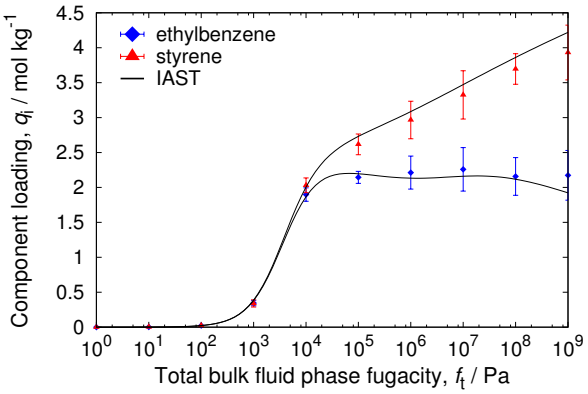

Figure S29: *Simulated mixture component isotherms in CoBDP at 433K.*

3

Selectivity in styrene/ethylbenzene equimolar mixture

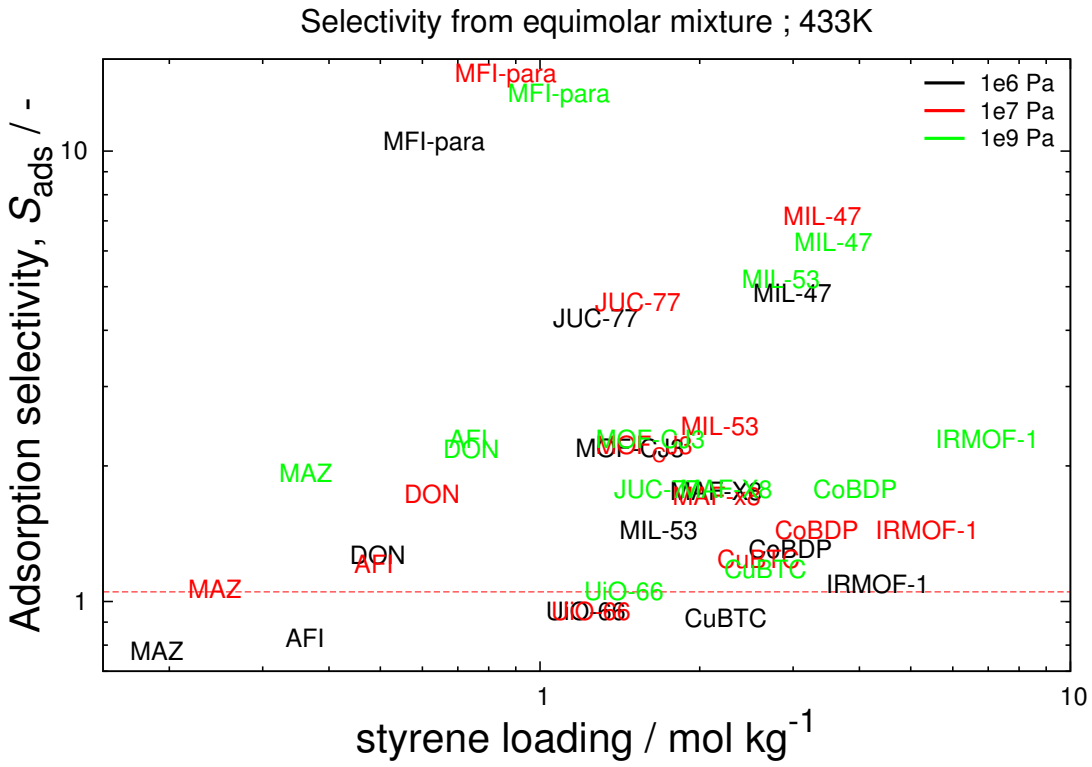

Figure S30: *Selectivity (q_{st}/q_{eb}) in an equimolar mixture at 3 different fugacities. The dashed red line corresponds to the liquid phase ratio. For all the cases styrene loading increases with the fugacity (shift to the right of the plot). The selectivity also increases in most of the cases with the fugacity (shift upwards) except for MFI-para, JUC-77, MIL-47 and Cu-BTC.*

3.1 Zeolites: small pore volumes

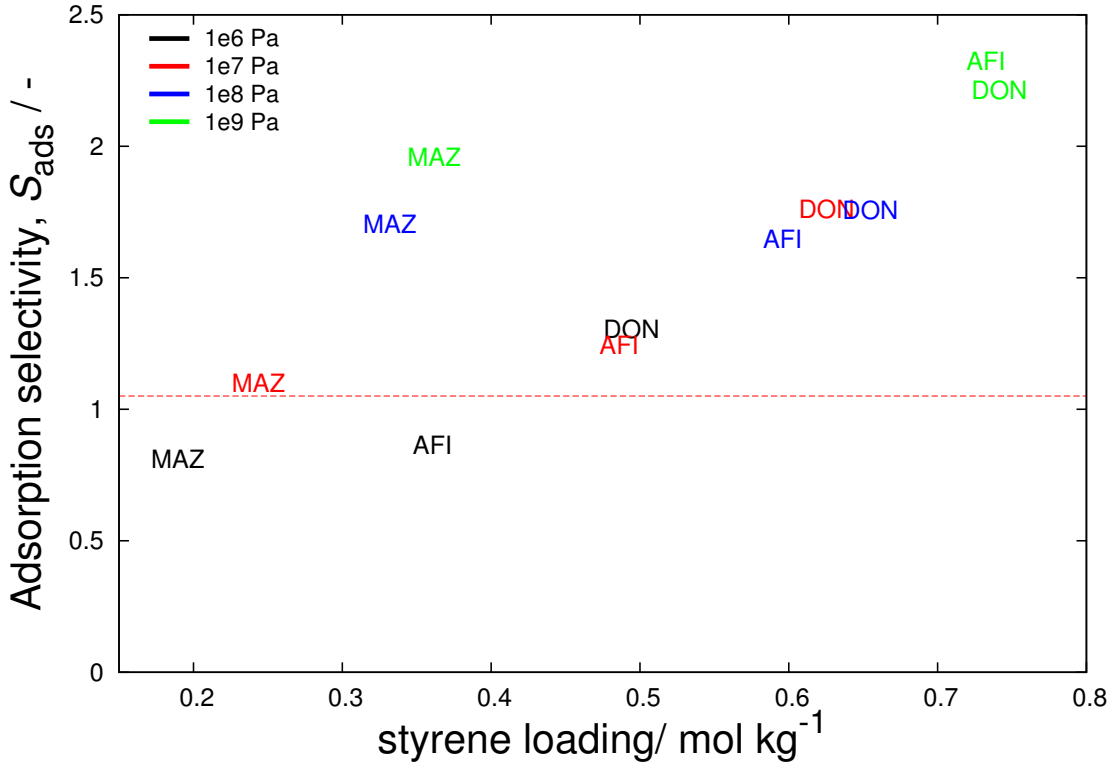

Figure S31: *Zoom in of Figure S30 in the zeolites region (low loading). The dashed red line corresponds to the liquid phase ratio.*

3.2 Interesting cases for the separation

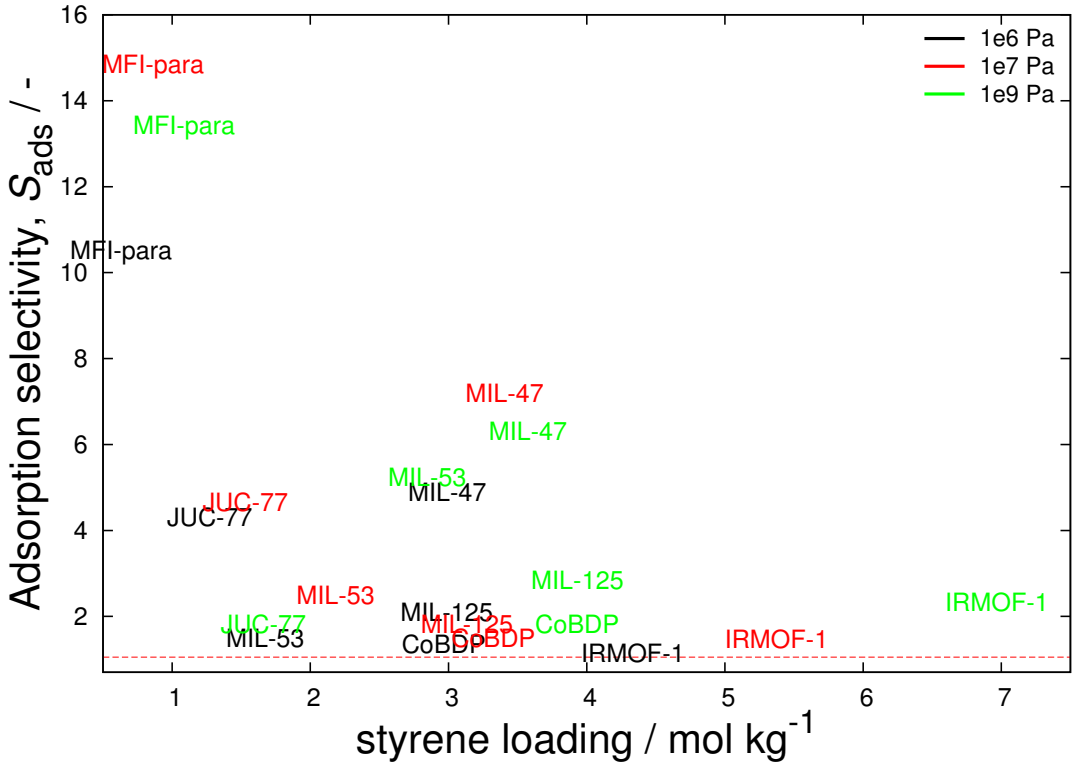

Figure S32: *Selectivity as a function of styrene loading for different fugacities in zeolites and metal-organic frameworks with interesting properties for the separation of styrene and ethylbenzene mixtures. The dashed red line corresponds to the liquid phase ratio.*

4

Screening of Potential Zeolite Adsorbents

4.1 AFI

unit cell size	$a = b = 13.827[\AA]$, $c = 8.58[\AA]$
unit cell angles	$\alpha = \beta = 90[°]$, $\gamma = 120[°]$
unit cells	$3 \times 3 \times 5$
framework density	1685.573 [kg/m^3]
description	AFI-type zeolite
crystallographic data	ref. [10]
void fraction	0.283131 [-]
accessible pore volume	0.1679 [cm^3/g]
nitrogen surface area	548 [m^2/g],924 [m^2/cm^3]
optimization	-
charges	REPEAT with PES from VASP

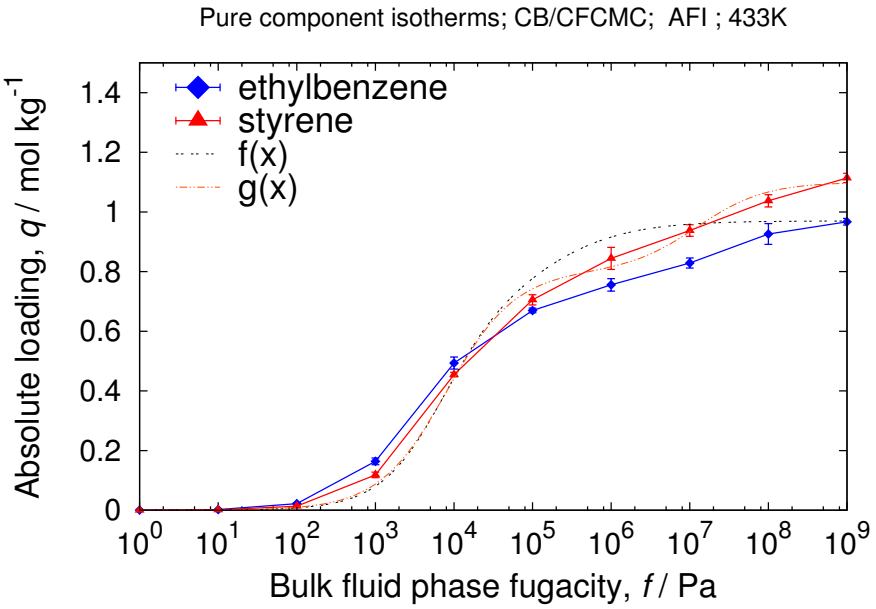

4.2 BEA

unit cell size	$a = b = 12.632[\AA]$, $c = 26.186[\AA]$
unit cell angles	$\alpha = \beta = \gamma = 90[^\circ]$
unit cells	$2 \times 2 \times 1$
framework density	1528.187 [kg/m^3]
description	BEA zeolite
crystallographic data	ref. [11]
void fraction	0.421281 [-]
accessible pore volume	0.2756 [cm^3/g]
nitrogen surface area	994 [m^2/g], 1519 [m^2/cm^3]
optimization	-
charges	REPEAT with PES from VASP

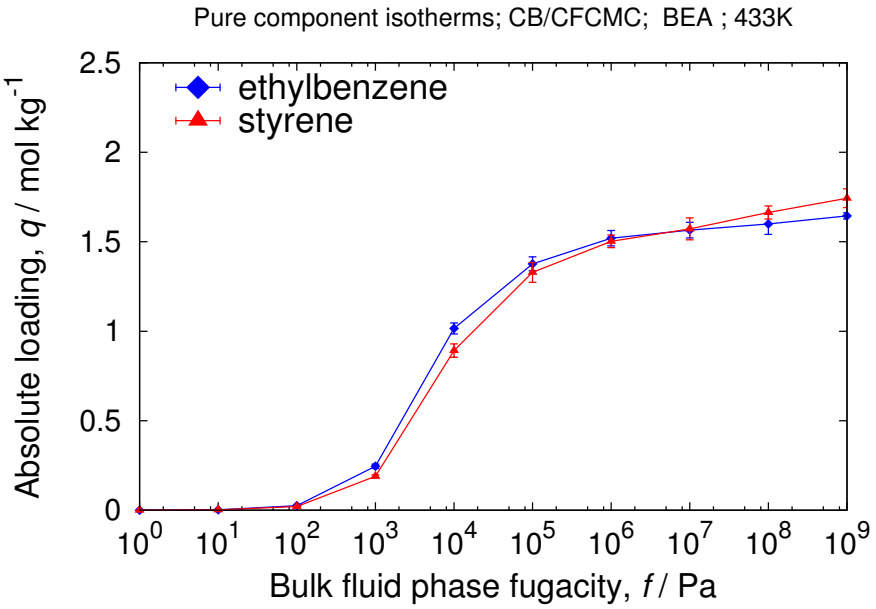

4.3 DON

unit cell size	$a = 18.89[\AA]$, $b = 23.365[\AA]$, $c = 8.46[\AA]$
unit cell angles	$\alpha = \beta = \gamma = 90[^\circ]$
unit cells	$2 \times 2 \times 4$
framework density	1708.2843 [kg/m^3]
description	DON zeolite
crystallographic data	ref. [12]
void fraction	0.287907 [-]
accessible pore volume	0.16853 [cm^3/g]
nitrogen surface area	525 [m^2/g], 897 [m^2/cm^3]
optimization	-
charges	REPEAT with PES from VASP

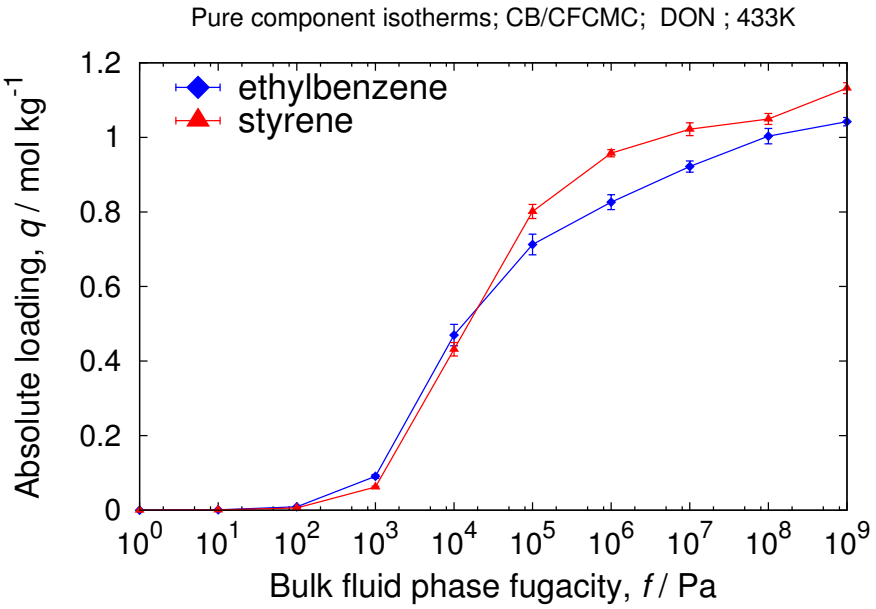

4.4 EMT

unit cell size	$a = b = 17.215[\AA]$, $c = 28.082[\AA]$
unit cell angles	$\alpha = \beta = 90[°]$, $\gamma = 120[°]$
unit cells	$2 \times 2 \times 1$
framework density	1328.9498 [kg/m^3]
description	EMT zeolite
crystallographic data	ref. [13]
void fraction	0.492004 [-]
accessible pore volume	0.3702 [cm^3/g]
nitrogen surface area	1136 [m^2/g], 1510 [m^2/cm^3]
optimization	-
charges	REPEAT with PES from VASP

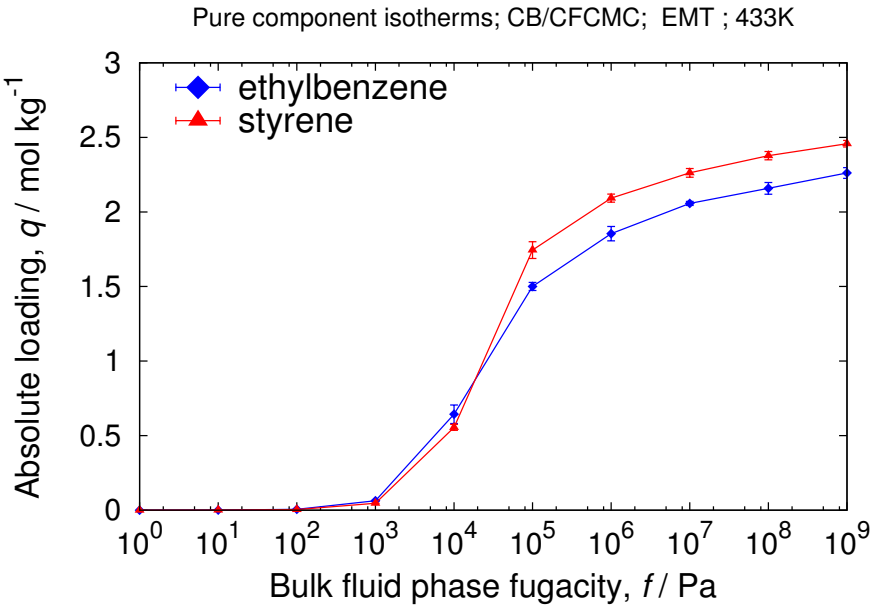

4.5 MAZ

unit cell size	$a = b = 18.1020[\AA]$, $c = 7.6180[\AA]$
unit cell angles	$\alpha = \beta = 90[°]$, $\gamma = 120[°]$
unit cells	$2 \times 2 \times 4$
framework density	1661.4522 [kg/m^3]
description	MAZ zeolite
crystallographic data	ref. [14]
void fraction	0.279375 [-]
accessible pore volume	0.1681 [cm^3/g]
nitrogen surface area	534 [m^2/g], 888 [m^2/cm^3]
optimization	-
charges	REPEAT with PES from VASP

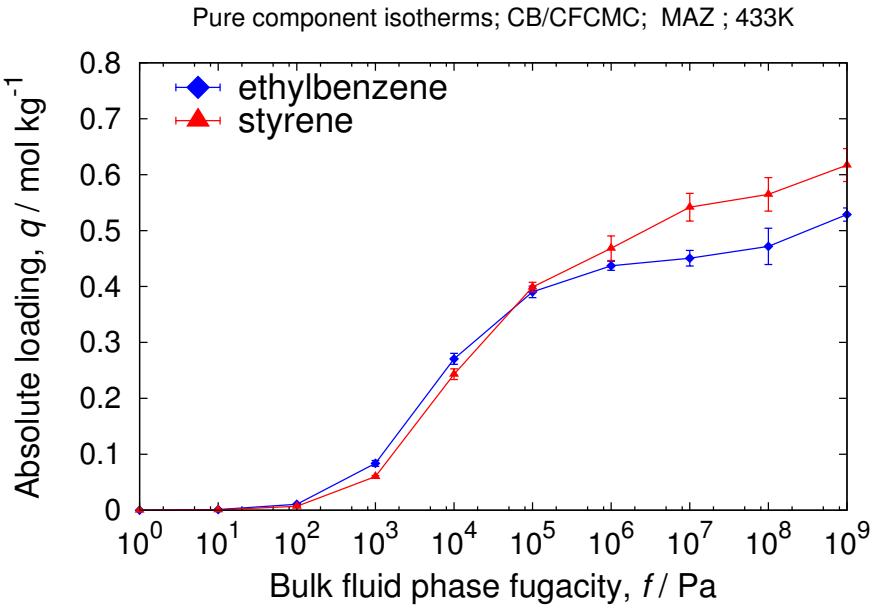

4.6 MFI(Olson)

unit cell size	$a = 20.07[\mathring{A}]$, $b = 19.92[\mathring{A}]$,$c = 13.42[\mathring{A}]$
unit cell angles	$\alpha = \beta = \gamma = 90[^\circ]$
unit cells	$2 \times 2 \times 2$
framework density	1785.2214 [kg/m^3]
description	MFI-Olson zeolite
crystallographic data	ref. [15]
void fraction	0.2988 [-]
accessible pore volume	0.16738 [cm^3/g]
nitrogen surface area	599 [m^2/g], 1069 [m^2/cm^3]
optimization	-
charges	REPEAT with PES from VASP

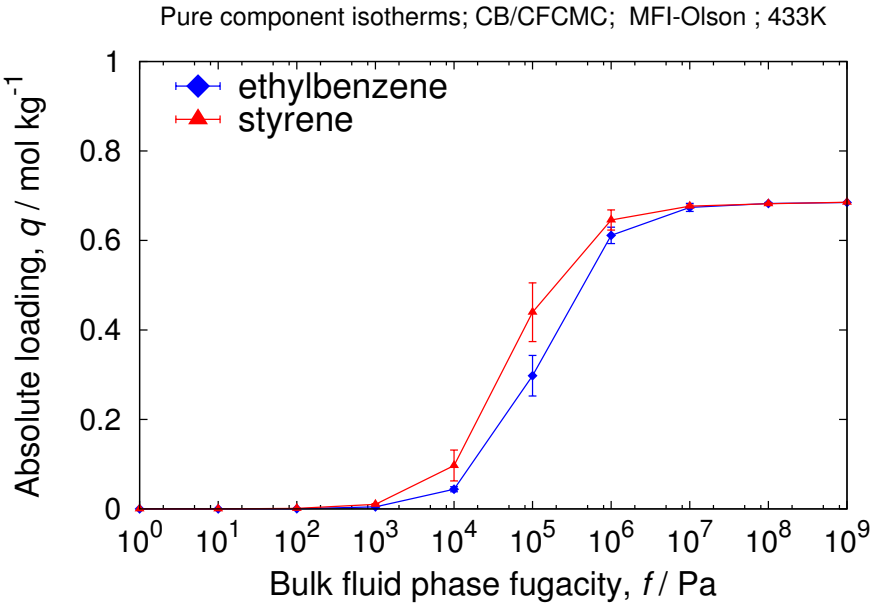

4.7 MFI(Van Koningsveld)

unit cell size	$a = 20.022, b = 19.899, c = 13.383[\AA]$
unit cell angles	$\alpha = \beta = \gamma = 90[^\circ]$
unit cells	$2 \times 2 \times 2$
framework density	1796.3424 [kg/m^3]
description	MFI zeolite
crystallographic data	ref. [16]
void fraction	0.294147 [-]
accessible pore volume	0.1637 [cm^3/g]
nitrogen surface area	584 [m^2/g], 1050 [m^2/cm^3]
optimization	-
charges	REPEAT with PES from VASP

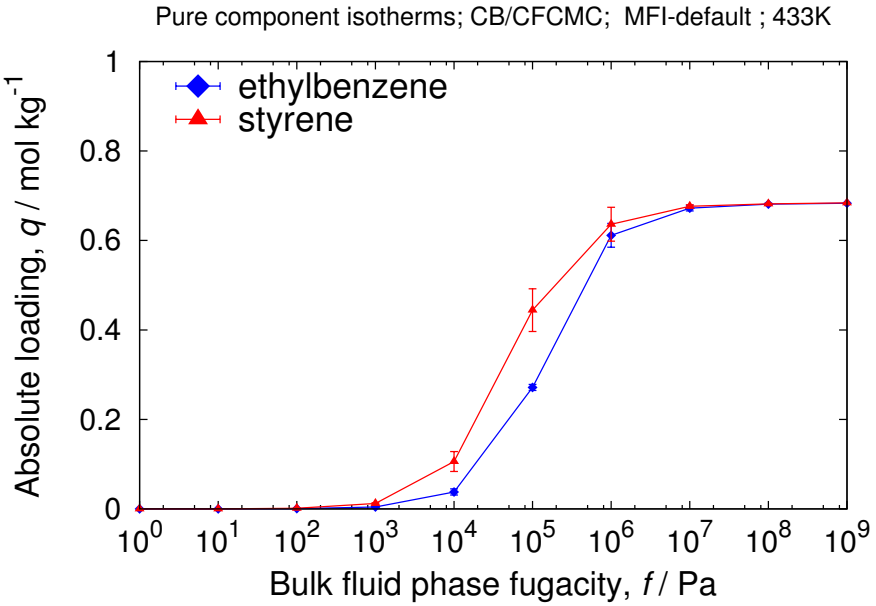

4.8 MFI-mono

unit cell size	$a = 20.1087[\AA], b = 19.879[\AA]$ [Å] $c = 8.58[\AA]$
unit cell angles	$\alpha = 90.67[^\circ]$, $\beta = \gamma = 90[^\circ]$
unit cells	$2 \times 2 \times 2$
framework density	1792.54[kg/m^3]
description	MFI-mono zeolite
crystallographic data	ref. [17]
void fraction	0.2860
accessible pore volume	0.1595
nitrogen surface area	663 [m^2/g],1188 [m^2/cm^3]
optimization	-
charges	REPEAT with PES from VASP

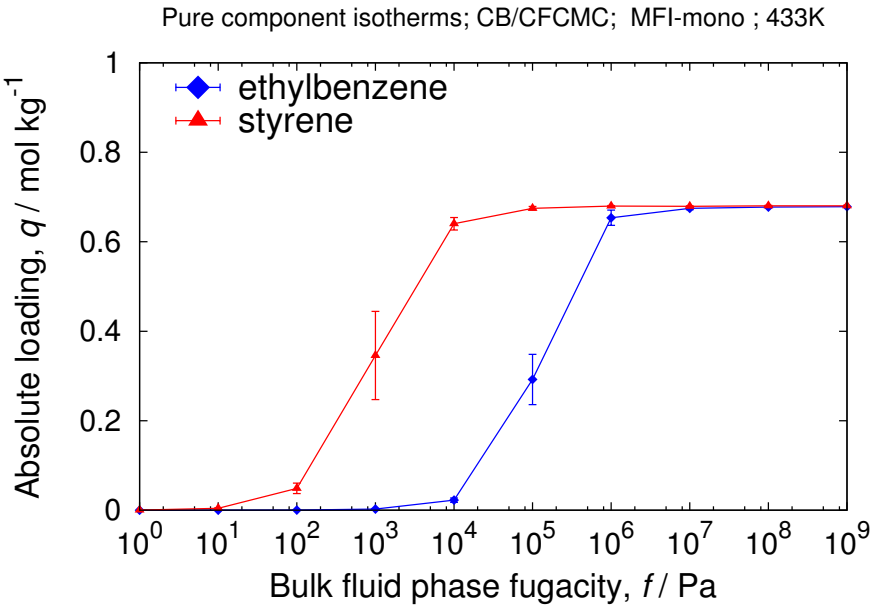

4.9 MFI-para

unit cell size	$a = 20.121[\AA]$, $b = 19.82[\AA]$,$c = 13.43[\AA]$
unit cell angles	$\alpha = \beta = \gamma = 90[^\circ]$
unit cells	$2 \times 2 \times 2$
framework density	1787.2835 [kg/m^3]
description	MFI-para zeolite
crystallographic data	ref. [18]
void fraction	0.278585 [-]
accessible pore volume	0.15587 [cm^3/g]
nitrogen surface area	602 [m^2/g], 1076 [m^2/cm^3]
optimization	-
charges	REPEAT with PES from VASP

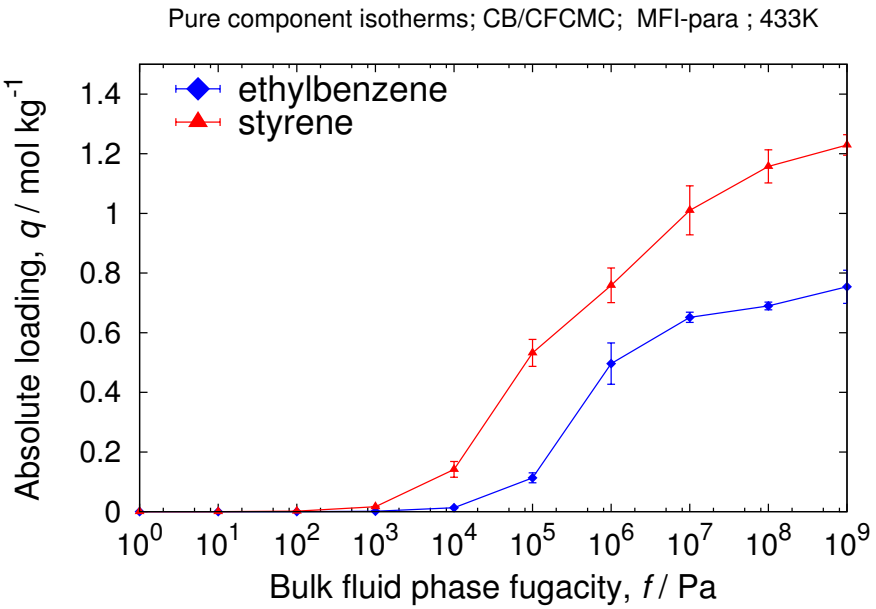

4.10 MOR

unit cell size	$a = 18.256, b = 20.534, c = 7.542[\AA]$
unit cell angles	$\alpha = \beta = \gamma = 90[^\circ]$
unit cells	$2 \times 2 \times 4$
framework density	1693.8915 [kg/m^3]
description	MOR zeolite
crystallographic data	ref. [19]
void fraction	0.267676 [-]
accessible pore volume	0.15802 [cm^3/g]
nitrogen surface area	994 [m^2/g], 1519 [m^2/cm^3]
optimization	-
charges	REPEAT with PES from VASP

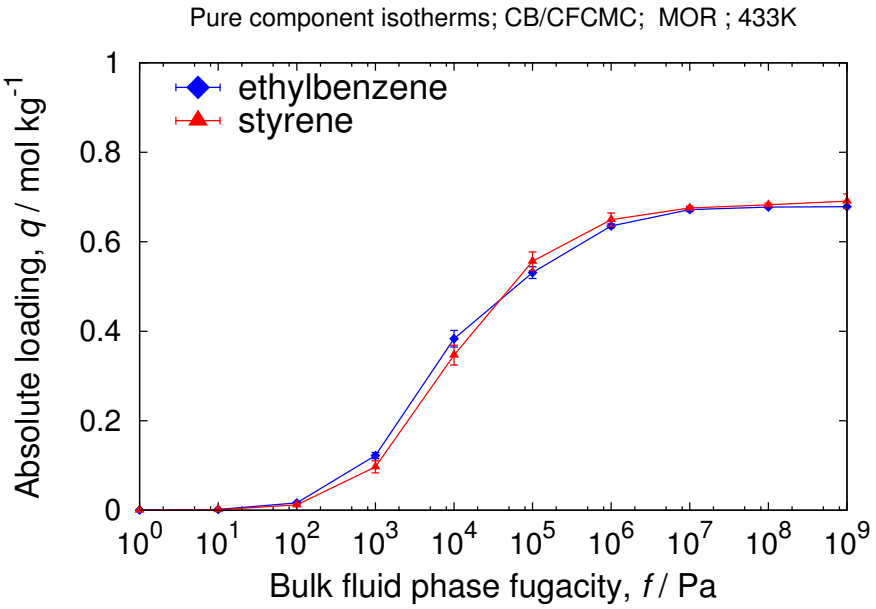

4.11 MRE

unit cell size	$a = 8.257[\AA]$, $b = 14.562[\AA]$, $c = 20.314[\AA]$
unit cell angles	$\alpha = \beta = \gamma = 90[^\circ]$
unit cells	$4 \times 2 \times 2$
framework density	1960.706 [kg/m^3]
description	MRE-type, ZSM-48
crystallographic data	ref. [20, 21]
void fraction	0.175396 [-]
accessible pore volume	0.0894 [cm^3/g]
nitrogen surface area	573 [m^2/g], 292 [m^2/cm^3]
optimization	-
charges	REPEAT with PES from VASP

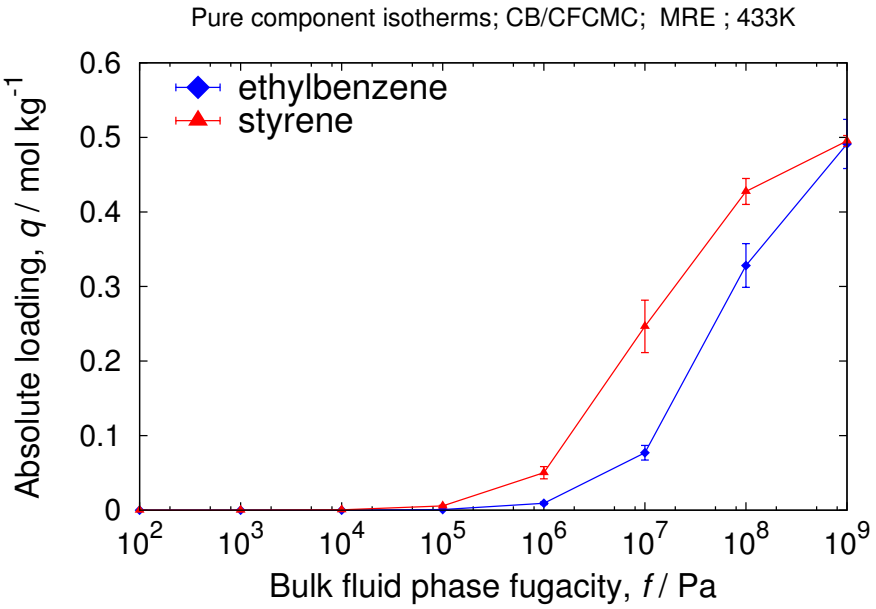

4.12 MTW

unit cell size	$a = 25.552[\AA]$, $b = 5.256[\AA]$, $c = 12.117[\AA]$
unit cell angles	$\alpha = 90[^\circ]$, $\beta = 109.312[^\circ]$, $\gamma = 90[^\circ]$
unit cells	$1 \times 6 \times 3$
framework density	1819.048 [kg/m^3]
description	MTW-type zeolite
crystallographic data	ref. [22]
void fraction	0.211619 [-]
accessible pore volume	0.11633 [cm^3/g]
nitrogen surface area	818 [m^2/g], 450 [m^2/cm^3]
optimization	-
charges	REPEAT with PES from VASP

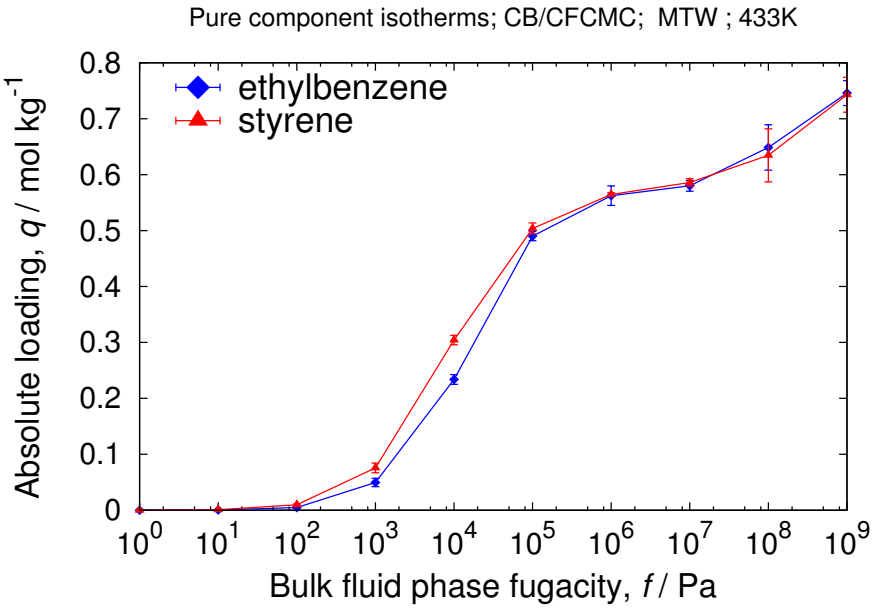

4.13 LTL

unit cell size	$a = b = 18.126[\AA], c = 7.56[\AA]$
unit cell angles	$\alpha = \beta = 90[^\circ], \gamma = 120[^\circ]$
unit cells	$2 \times 2 \times 4$
framework density	1668.2235 [kg/m^3]
description	LTL zeolite
crystallographic data	ref. [23]
void fraction	0.5193 [-]
accessible pore volume	0.3115 [cm^3/g]
nitrogen surface area	550 [m^2/g], 918 [m^2/cm^3]
optimization	-
charges	REPEAT with PES from VASP

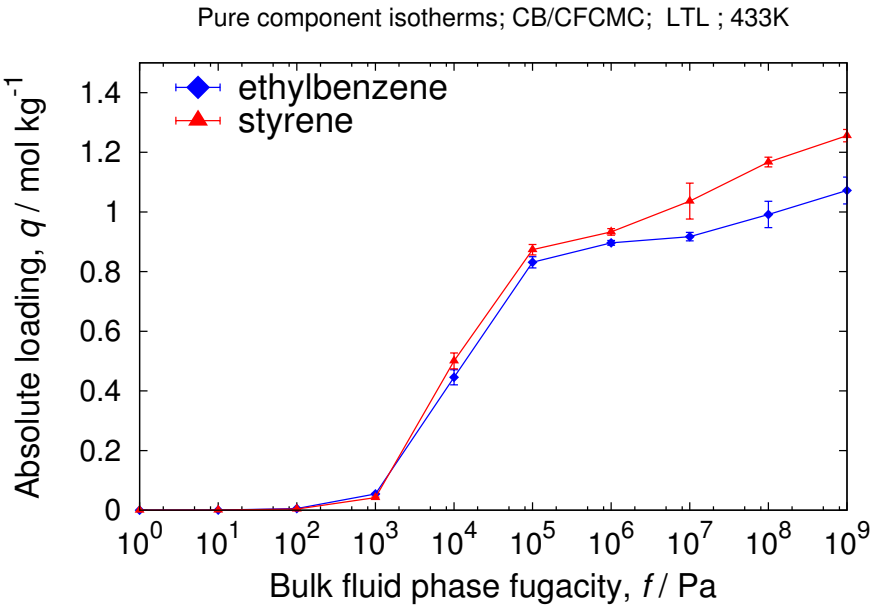

5

Screening of Potential MOF Adsorbents

5.1 CoBDP

unit cell size	$a = 13.253[\AA]$, $b = 13.253[\AA]$, $c = 13.995[\AA]$
unit cell angles	$\alpha = \beta = \gamma = 90[^\circ]$
unit cells	$2 \times 2 \times 3$
framework density	721.88 [kg/m^3]
description	Co(BDP)
crystallographic data	ref. [24]
void fraction	0.6535 [-]
accessible pore volume	0.9053 [cm^3/g]
nitrogen surface area	2244 [m^2/g], 1620 [m^2/cm^3]
optimization	VASP fixed cell, PBE, precision=high
charges	REPEAT with PES from VASP

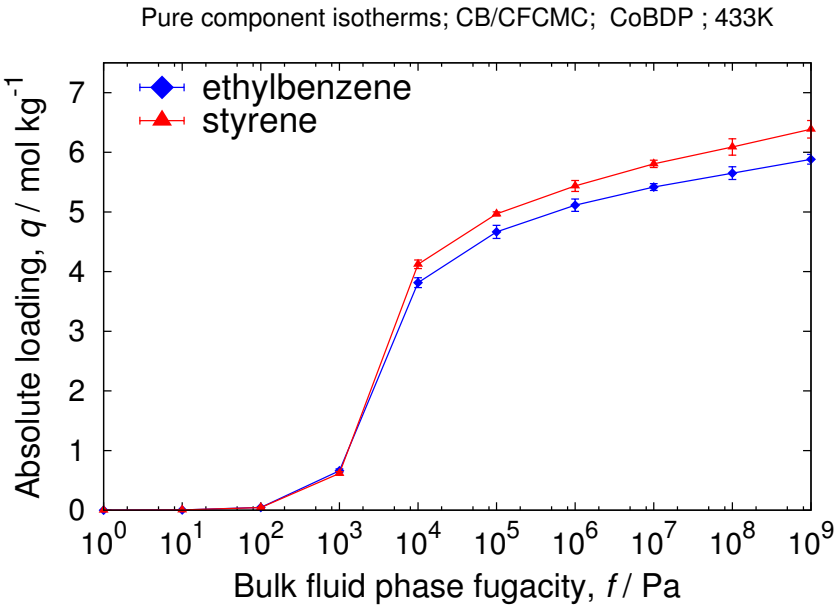

5.2 CoDOBDC

unit cell size	$a = 25.885[\AA]$, $b = 25.885[\AA]$, $c = 6.8058[\AA]$
unit cell angles	$\alpha = \beta = 90, \gamma = 120[^\circ]$
unit cells	$2 \times 2 \times 4$
framework density	1180.56 [kg/m^3]
description	Co(DOBDC)
crystallographic data	ref. [25]
void fraction	0.706 [-]
accessible pore volume	0.59811 [cm^3/g]
nitrogen surface area	1338[m^2/g], 1580[m^2/cm^3]
optimization	-
charges	REPEAT with PES from VASP

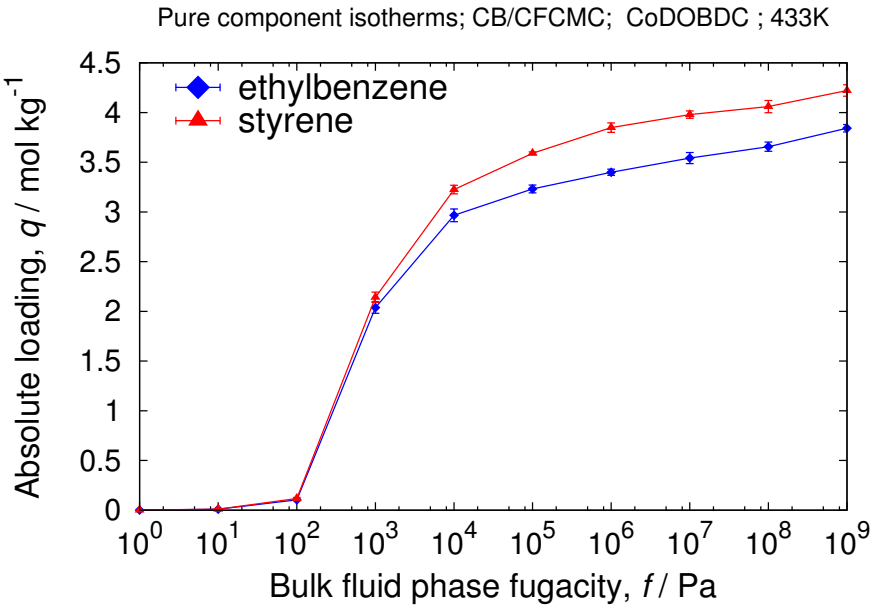

5.3 Cu-BTC

unit cell size	$a = b = c = 18.6273[\AA]$
unit cell angles	$\alpha = \beta == 60[°]$
unit cells	$2 \times 2 \times 2$
framework density	1685.573 [kg/m^3]
description	Cu-BTC
crystallographic data	ref. [26]
void fraction	0.283131 [-]
accessible pore volume	0.1679 [cm^3/g]
nitrogen surface area	548 [m^2/g],924 [m^2/cm^3]
optimization	-
charges	REPEAT with PES from VASP

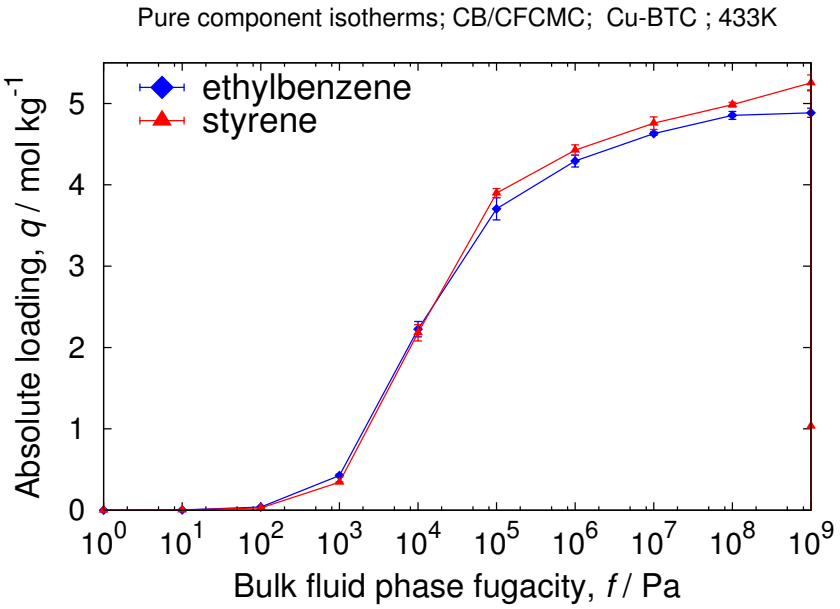

5.4 IRMOF-1

unit cell size	$a = b = c = 18.2660[\AA]$
unit cell angles	$\alpha = \beta = \gamma = 60[^\circ]$
unit cells	$2 \times 2 \times 2$
framework density	593.394 [kg/m^3]
description	IRMOF-1
crystallographic data	ref. [27]
void fraction	0.8038[-]
accessible pore volume	0.9271[cm^3/g]
nitrogen surface area	3592 [m^2/g], 2131 [m^2/cm^3]
optimization	-
charges	REPEAT with PES from VASP

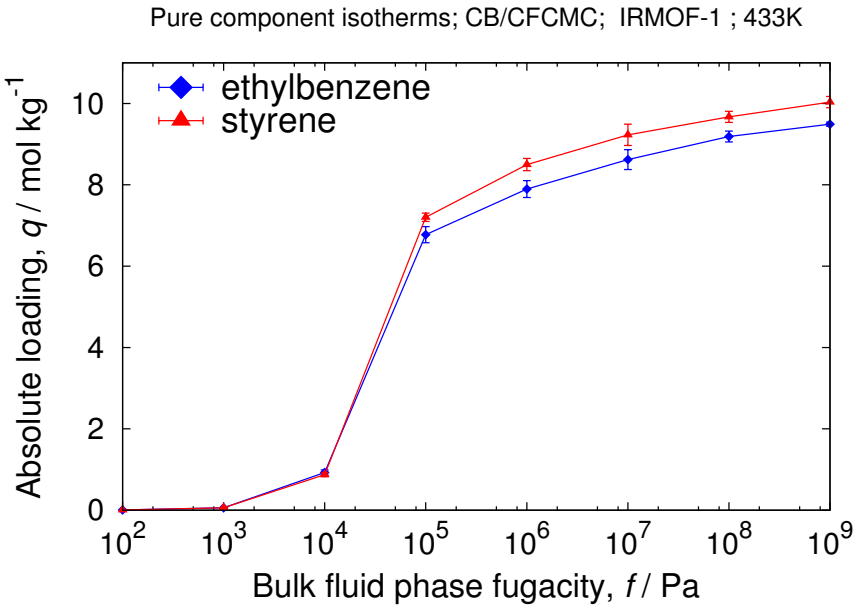

5.5 JUC-77

unit cell size	$a = 13.985[\AA]$, $b = 25.205[\AA]$, $c = 24.996[\AA]$
unit cell angles	$\alpha = 32.34, \beta = 74.65, \gamma = 73.003[^\circ]$
unit cells	$2 \times 2 \times 2$
framework density	1144.03 [kg/m^3]
description	JUC-77
crystallographic data	ref. [28]
void fraction	0.4783 [-]
accessible pore volume	0.4181 [cm^3/g]
nitrogen surface area	1098 [m^2/g], 1256 [m^2/cm^3]
optimization	VASP fixed cell, PBE, precision=high
charges	REPEAT with PES from VASP

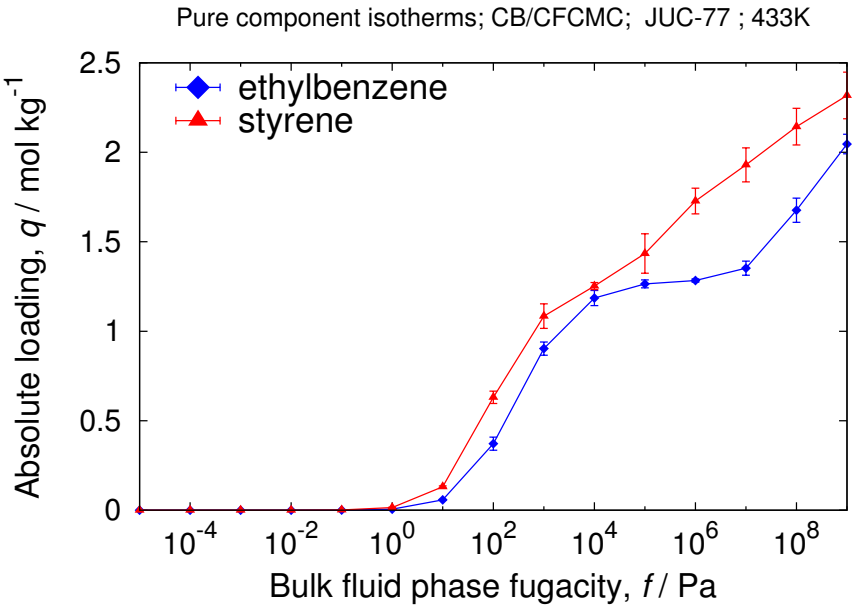

5.6 MAF-X8

unit cell size	$a = 13.9249[\AA]$, $b = 23.653[\AA]$, $c = 23.637[\AA]$
unit cell angles	$\alpha = \beta = \gamma = 90[^\circ]$
unit cells	$2 \times 2 \times 2$
framework density	954.2915 [kg/m^3]
description	MAF-x8
crystallographic data	ref. [29]
void fraction	0.4947[-]
accessible pore volume	0.5184 [cm^3/g]
nitrogen surface area	1465 [m^2/g], 1397 [m^2/cm^3]
optimization	-
charges	REPEAT with PES from VASP

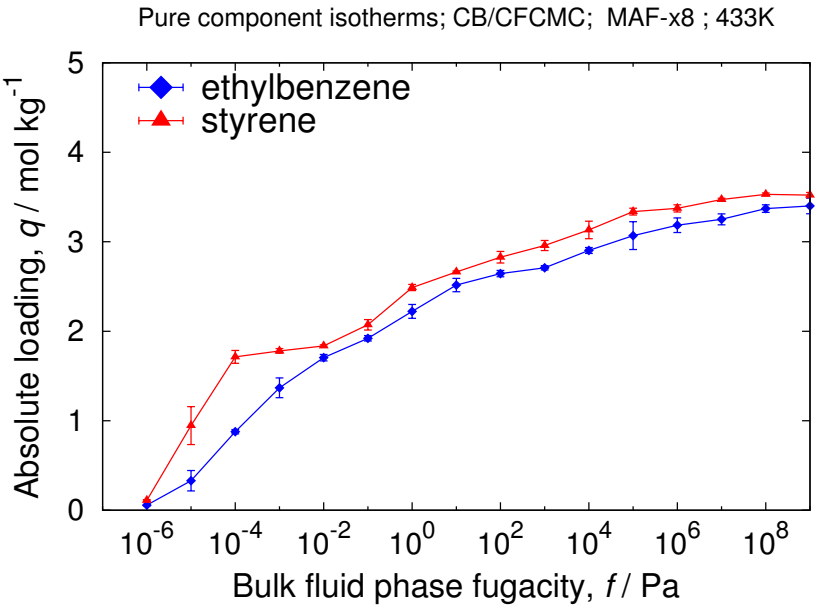

5.7 MIL-47

unit cell size	$a = 6.8179[\AA]$, $b = 16.143[\AA]$, $c = 13.939[\AA]$
unit cell angles	$\alpha = \beta = \gamma = 90[^\circ]$
unit cells	$4 \times 2 \times 2$
framework density	1000.36 [kg/m^3]
description	MIL-47
crystallographic data	ref. [30]
void fraction	0.6088 [-]
accessible pore volume	0.6086 [cm^3/g]
nitrogen surface area	1655 [m^2/g], 1656 [m^2/cm^3]
optimization	-
charges	REPEAT with PES from VASP

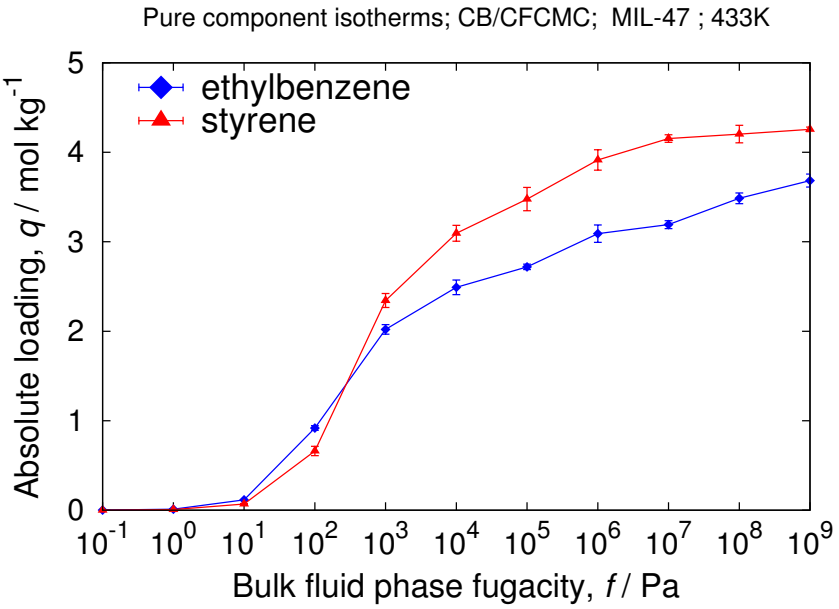

5.8 MIL-53

unit cell size	$a = 16.73300[\AA]$, $b = 13.038[\AA]$, $c = 6.8120[\AA]$
unit cell angles	$\alpha = \beta = \gamma = 90[^\circ]$
unit cells	$2 \times 2 \times 4$
framework density	$1041.90[kg/m^3]$
description	MIL-53
crystallographic data	ref. [31]
void fraction	0.5501[-]
accessible pore volume	$0.5279[cm^3/g]$
nitrogen surface area	$1435[m^2/g]$,$1495[m^2/cm^3]$
optimization	-
charges	REPEAT with PES from VASP

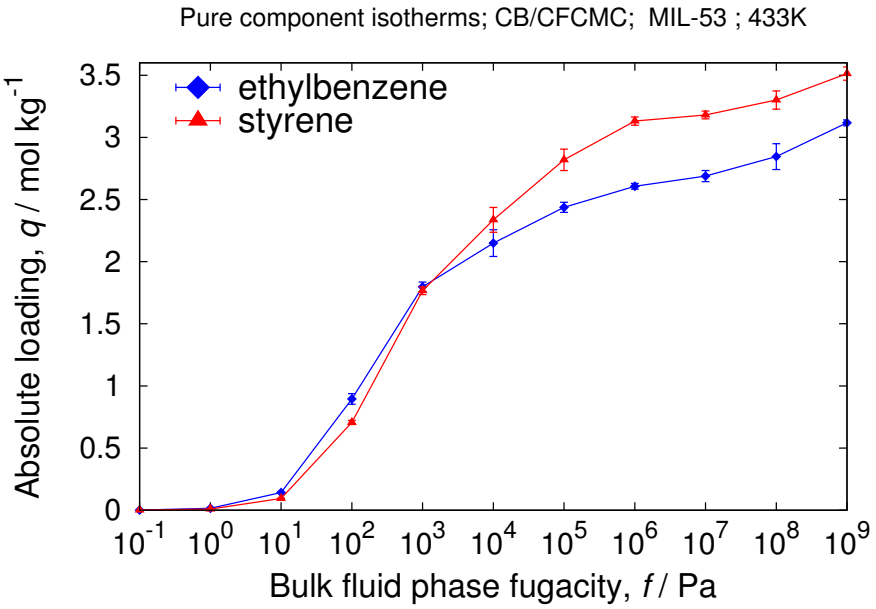

5.9 MIL-125

unit cell size	$a = 18.65430[\AA]$, $b = 18.65430[\AA]$,$c = 18.1444[\AA]$
unit cell angles	$\alpha = \beta = \gamma = 90[^\circ]$
unit cells	$2 \times 2 \times 2$
framework density	[kg/m^3]
description	MIL-125
crystallographic data	ref. [32]
void fraction	0.620306 [-]
accessible pore volume	0.7542 [cm^3/g]
nitrogen surface area	2231.447617[m^2/g],1835.290387 [m^2/cm^3]
optimization	VASP fixed cell, PBE, precision=high
charges	REPEAT with PES from VASP

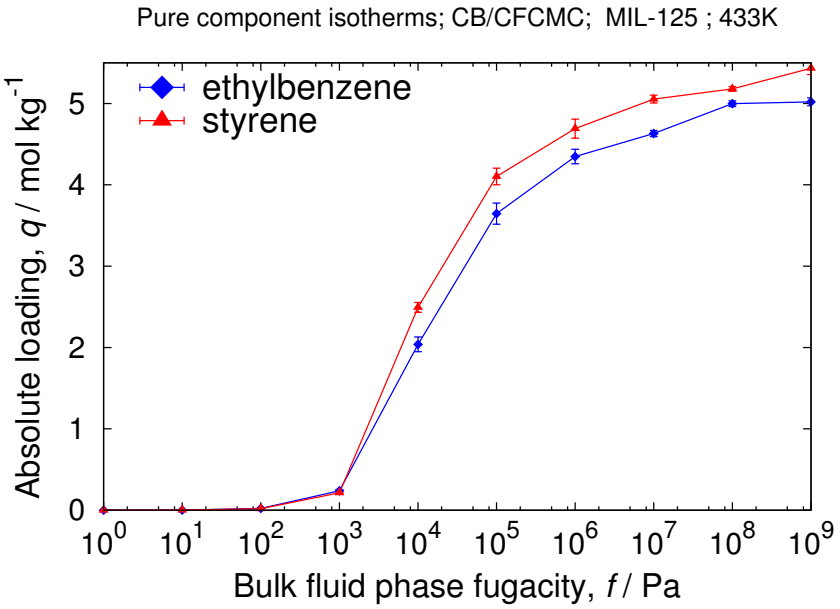

5.10 MIL-125-NH_2

unit cell size	$a = b = 18.729[\AA]$, $c = 18.172[\AA]$
unit cell angles	$\alpha = \beta = \gamma = 90[^\circ]$
unit cells	$2 \times 2 \times 2$
framework density	861.6161 [kg/m^3]
description	MIL-125
crystallographic data	ref. [33]
void fraction	0.5921 [-]
accessible pore volume	0.6872 [cm^3/g]
nitrogen surface area	[m^2/g], [m^2/cm^3]
optimization	VASP fixed cell, PBE, precision=high
charges	REPEAT with PES from VASP

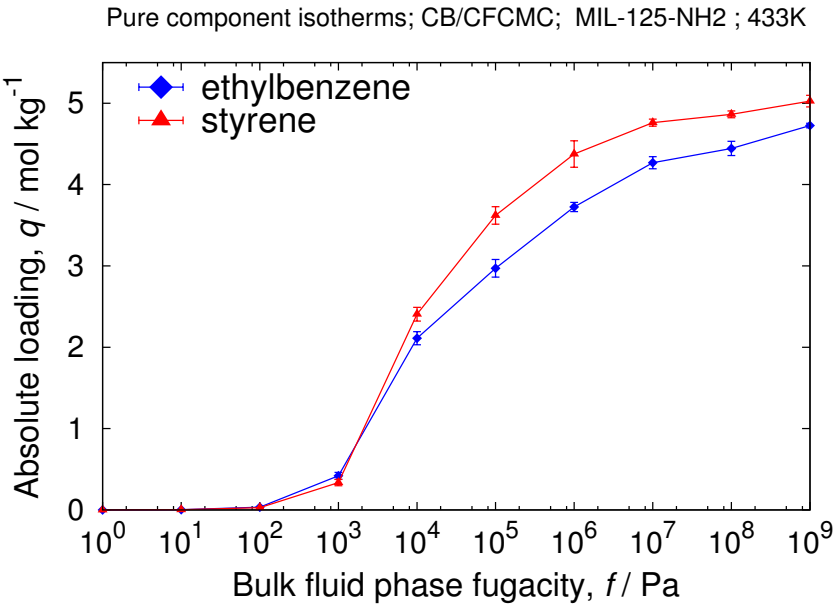

5.11 MOF-CJ3

unit cell size	$a = 20.588[\AA]$, $b = 20.588[\AA]$, $c = 17.832[\AA]$
unit cell angles	$\alpha = \beta = \gamma = 90[^\circ]$
unit cells	$2 \times 2 \times 4$
framework density	954.2909 [kg/m^3]
description	MOF-CJ3
crystallographic data	ref. [34]
void fraction	0.4478[-]
accessible pore volume	0.3440 [cm^3/g]
nitrogen surface area	870 [m^2/g], 1133 [m^2/cm^3]
optimization	VASP fixed cell, PBE, precision=high
charges	REPEAT with PES from VASP

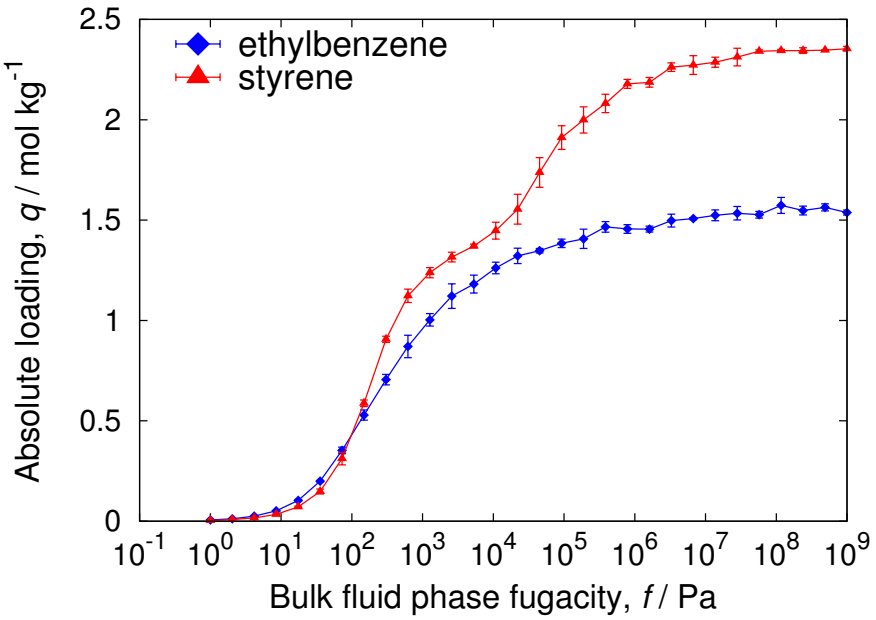

5.12 NiDOBDC

unit cell size	$a = 25.7856[\AA]$, $b = 25.7856[\AA]$, $c = 6.7701[\AA]$
unit cell angles	$\alpha = \beta = 90, \gamma = 120[^\circ]$
unit cells	$2 \times 2 \times 4$
framework density	1194.120 [kg/m^3]
description	NiDOBDC
crystallographic data	ref. [35]
void fraction	0.6931[-]
accessible pore volume	0.5804 [cm^3/g]
nitrogen surface area	1311 [m^2/g], 1566 [m^2/cm^3]
optimization	-
charges	REPEAT with PES from VASP

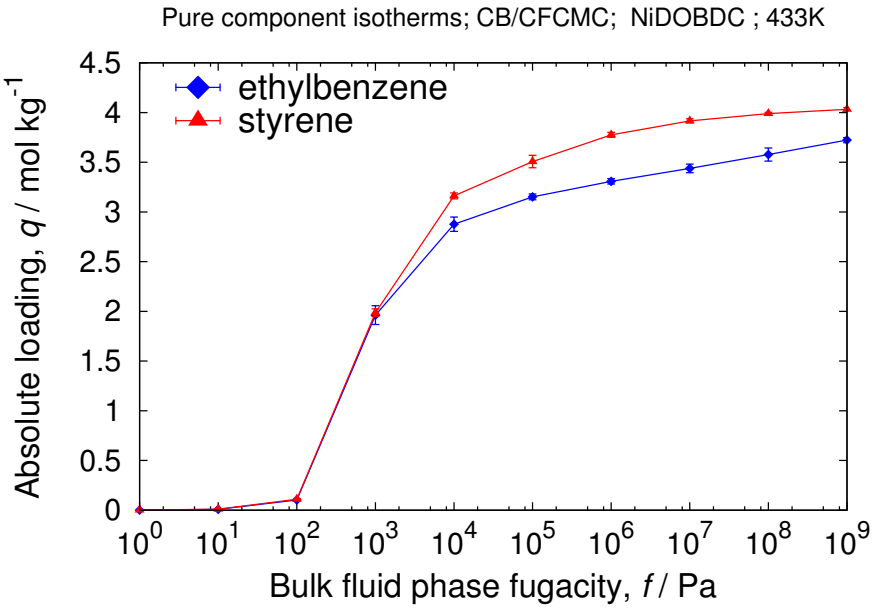

5.13 UiO-66

unit cell size	$a = b = c = 20.7004[\AA]$
unit cell angles	$\alpha = \beta = \gamma = 90[^\circ]$
unit cells	$2 \times 2 \times 2$
framework density	$1219.0883[kg/m^3]$
description	UiO-66
crystallographic data	ref. [36]
void fraction	0.496497 [-]
accessible pore volume	0.40718 [cm^3/g]
nitrogen surface area	1116 [m^2/g], 1360 [m^2/cm^3]
optimization	-
charges	REPEAT with PES from VASP

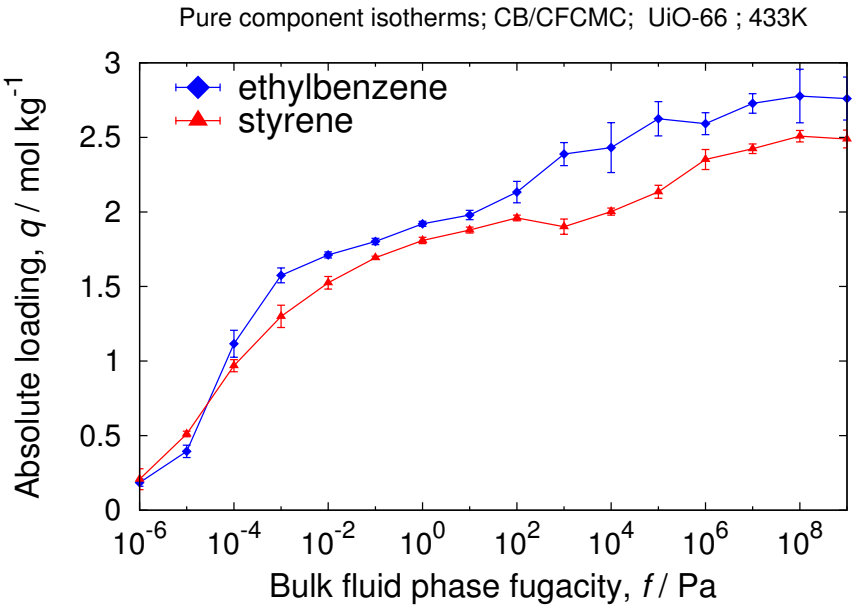

5.14 ZnDOBDC

unit cell size	$a = b = 25.9320[\AA]$, $c = 6.8365[\AA]$
unit cell angles	$\alpha = \beta = 90, \gamma = 120[^\circ]$
unit cells	$2 \times 2 \times 4$
framework density	1219.604 [kg/m^3]
description	ZnDOBDC
crystallographic data	ref. [37]
void fraction	0.71931[-]
accessible pore volume	0.5898 [cm^3/g]
nitrogen surface area	1289 [m^2/g], 1572 [m^2/cm^3]
optimization	-
charges	REPEAT with PES from VASP

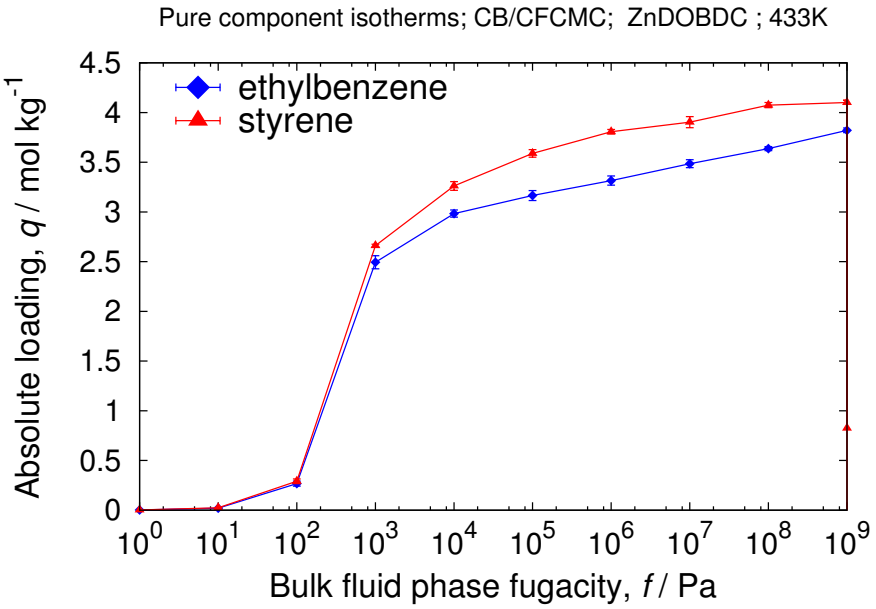

Bibliography

[1] Torres-Knoop, A.; Balaji, S. P.; Vlugt, T.; Dubbeldam, D. *J. Chem. Theory Comput* **2014**, *10*, 942–952.

[2] Siepmann, J. *Mol. Phys.* **1990**, *70*, 1145–1158.

[3] Siepmann, J.; Frenkel, D. *Mol. Phys.* **1992**, *75*, 59–70.

[4] Frenkel, D.; Mooij, G.; Smit, B. *J. Phys.: Condens. Matter* **1992**, *4*, 3053–3076.

[5] Shi, W.; Maginn, E. *J. Chem. Theory Comput.* **2007**, *3*, 1451–1463.

[6] Shi, W.; Maginn, E. *J. Comput. Chem.* **2008**, *29*, 2520–2530.

[7] Dubbeldam, D.; Knoop, A.; Walton, K. *Mol. Simulat.* **2013**, *39*, 1253–1292.

[8] Martin, M.; Siepmann, J. *J. Am. Chem. Soc.* **1997**, *119*, 8921–8924.

[9] Panagiotopoulos, A. *Int. J. Thermophys.* **1989**, *10*, 447–457.

[10] Qiu, S.; Pang, W.; Kessler, H.; Guth, J. *Zeolites* **1989**, *9*, 440–444.

[11] Newsam, J.; Treacy, M.; Koetsier, W. T.; de Gruyter, C. *Proc. Roy. Soc. A (London)* **1988**, *420*, 375–405.

[12] Wessels, T.; Baerlocher, C.; McCusker, L.; Creyghton, E. *J. Am. Chem. Soc.* **1999**, *121*, 6242–6247.

[13] Baerlocher, C.; McCusker, L.; Chiappetta, R. *Microporous Mater.* **1994**, *2*, 269–280.

[14] Galli, E. *Rend. Soc. Ital. Mineral. Petrol.* **1975**, *31*, 599–612.

[15] Olson, D.; Kokotailo, G.; Lawton, S.; Meier, W. *J. Phys. Chem.* **1981**, *85*, 2238–2243.

[16] van Koningsveld, H.; van Bekkum, H.; Jansen, J. *Acta Cryst. B* **1987**, *43*, 127–132.

[17] van Koningsveld, H.; Jansen, J. C.; ; van Bekkum, H. *Zeolites* **1990**, *10*, 235–242.

[18] van Koningsveld, H.; et al, *Acta. Cryst.* **1989**, *B45*, 423–431.

[19] Gramlich, V. *Ph.D. Thesis, ETH, Zürich, Switzerland* **1971**,

[20] Schlenker, J.; J.L.,; Rohrbaugh,; W.J.,; Chu,; P.,; Valyocsik,; E.W.,; Kokotailo, G. T. *Zeolites* **1985**, *5*, 355–358.

[21] Lobo, R.; van Koningsveld, H. *J. Am. Chem. Soc.* **2002**, *124*, 13222–13230.

[22] Fyfe, C.; Gies, H.; Kokotailo, G.; Marler, B.; ; Cox, D. *J. Phys. Chem.* **1990**, *94*, 3718–3721.

[23] Newsam, J. *J. Phys. Chem.* **1989**, *93*, 7689–7694.

[24] H.J. Choi, M. D.; Long, J. *J. Am. Chem. Soc.* **2008**, *130*, 7848–7850.

[25] Dietzel, P.; Morita, Y.; Blom, R.; Fjellvag, H. *Angew. Chem. Int. Ed* **2005**, *44*, 6354.

[26] Chui, S. S.-Y.; Lo, S. M.-F.; Charmant, J. P. H.; Orpen, A. G.; Williams, I. D. *Science* **1999**, *283*, 1148–1150.

[27] Li, H.; Eddaoudi, M.; O'Keeffe, M.; Yaghi, O. M. *Nature* **1999**, *402*, 276.

[28] Jin, Z.; Zhao, H.-Y.; Zhao, X.-J.; Fang, Q.-R.; Long, J.; Zhu, G.-S. *Chem. Comm* **2010**, *46*, 8612–8614.

[29] He, C.-T.; Tian, J.-Y.; Liu, S.-Y.; Ouyang, G.; Zhang, J.-P.; Chen, X.-M. *Chem. Sci.* **2013**, *4*, 351–356.

[30] Barthelet, K.; Marrot, J.; Riou, D.; Ferey, G. *Ang. Chem. Int. Ed.* **2002**, *41*, 281–284.

[31] Serre, C.; Millange, F.; Thouvenot, C.; Nogues, M.; Marsolier, G.; Louer, D.; Ferey, G. *J. Am. Chem. Soc.* **2002**, *124*, 13519–13526.

[32] Dan-Hardi, M.; Serre, C.; Frot, T.; Rozes, L.; Maurin, G.; Sanchez, C.; Ferey, G. *J. Am. Chem. Soc.* **2009**, *131*, 10857–10859.

[33] Fu, Y.; Sun, D.; Chen, Y.; Huang, R.; Ding, Z.; Fu, X.; Li, Z. *Angew. Chem. Int. Ed.* **2012**, *124*, 3420–3423.

[34] Fang, Z.; Zheng, S.; Tan, J.; Cai, S.; Fan, J.; Yan, X.; Zhang, W. *Journal of Chromatography A* **2013**, 132–8.

[35] Dietzel, P.; Panella, B.; Hirscher, M.; Blom, R.; Fjellvag, H. *Chem. Comm* **2006**, 959.

[36] Cavka, J.; Jakobsen, S.; Olsbye, U.; Guillou, N.; Lamberti, C.; Bordiga, S.; Lillerud, K. *J. Am. Chem. Soc.* **2008**, *130*, 13850–13851.

[37] Rowsell, J.; O.M.Yaghi, *J. Am. Chem. Soc* **2006**, *128*, 1304.